

Ram Prakash, T. Pütterich, R. Dux, A. Kallenbach, R. Fischer, K.
Behringer, ASDEX Upgrade Team

Spectroscopic Divertor Characterization and Impurity Influx Measurements in ASDEX Upgrade Tokamak

**IPP 10/31
September, 2006**

Spectroscopic Divertor Characterization and Impurity Influx Measurements in ASDEX Upgrade Tokamak

Ram Prakash*, T. Pütterich, R. Dux, A. Kallenbach, R. Fischer, K. Behringer
ASDEX Upgrade Team

*Max-Planck-Institut für Plasmaphysik, EURATOM Assoc., D-85748 Garching,
Germany*

**Birla Institute of Technology, 27-Malviya Industrial Area, Jaipur-302017, India*

Abstract

A spectroscopic characterization of the divertor plasma in the ASDEX Upgrade tokamak is presented for ohmic and H-mode experiments with main emphasis on plasma density and temperature measurements. Using Stark broadening tabulations, we have developed a chi-square fit procedure with the Balmer series D_δ and D_γ lines to infer the average electron density in the divertor plasma. The densities are obtained from the fit procedure through a probability analysis. The center of the probability distribution function confers the estimated density whereas its half-width determines its uncertainty. The relative uncertainties are tested by comparing derived density values of D_δ with D_γ line. In addition to the electron density estimation from Stark broadening, a simultaneous fit of the deuterium Balmer series D_β , D_γ , D_δ , D_ϵ line intensities with ADAS collisional-radiative (CR) model data allows in determining the effective electron temperature, the average ground state atom and ion densities. A couple of boron and helium line ratios are found useful which can be utilized to derive the effective electron temperature in the Divertor region. However, a clear disagreement is observed for recombining plasma cases where temperature estimations from the CR-model fitting and these ratios do not match. This observation puts doubts on the applicability of the line ratio method for divertor conditions. On the basis of estimated basic plasma parameters and subsequently derived S/XB values from ADAS database, the impurity influx measurements for ohmic discharges are carried out. In comparison to the ion fluxes at the target, helium ground state and deuterium fluxes are increased during recombining phase whilst fluxes of boron, carbon and oxygen have reduced drastically. The particle fluxes obtained from spectroscopy lies within a factor of two than that from Langmuir probe, but the estimated plasma densities are around one order of magnitude larger. Detached plasmas are observed during ohmic discharges. The found degree of detachment is ~ 4 . During detached divertor conditions, the plasma temperature has dropped from 7-10 eV to ~ 2 eV in the outer divertor region.

1. Introduction:

This research report is an outcome of the work carried out at ASDEX Upgrade tokamak under BOYSCAST fellowship scheme of Govt. of India. The overall motivation of this work was to execute quantitative studies on plasma spectroscopy and impurity transports in tokamak plasmas. The tokamak is based at Max-Planck Institute for Plasma Physics, Garching near Munich, Germany. ASDEX Upgrade (AUG) [1] is a divertor tokamak with typical major plasma radius 1.65 m, minor vertical plasma radius 0.8 m and minor horizontal plasma radius 0.5 m. A typical poloidal cross-section of the plasma used for this work is shown in the figure 1. AUG can operate in deuterium or hydrogen plasmas. For this work deuterium plasmas were studied. The important part of the experimental program of AUG is devoted to the study of plasma-wall interaction in different scenarios related for the next step device ITER [2-3]. These include standard and improved H-mode (high confinement mode) as well as detached divertor operations. During 2006 campaign under investigation 85 % of the Plasma Facing Components (PFC's) in AUG were coated with tungsten.

A key issue for design and construction of controlled thermonuclear fusion reactors is the interaction of hot plasma with the PFC's [4-5]. It is due to the fact that the bombardment of the wall elements by particles escaping the plasma or streaming along field lines in turn produces a source of neutral atoms from the wall materials. Depending on the location of the surface and plasma properties in the vicinity of the source, a certain fraction of the wall atoms then penetrate to the main plasma. The presence of such non-hydrogenic atoms and commonly occurring ions of these impurity elements dilutes the plasma and is of major concern; the impurities contribute significantly to the plasma radiation losses which adversely affect the plasma performance. The contamination of the plasma by impurities released from the vessel structure is thus one of the major problems caused by the plasma wall interaction. To understand the impurity behavior during such interactions, the basic plasma parameters and impurity influxes from the most susceptible regions of the plasma have to be obtained.

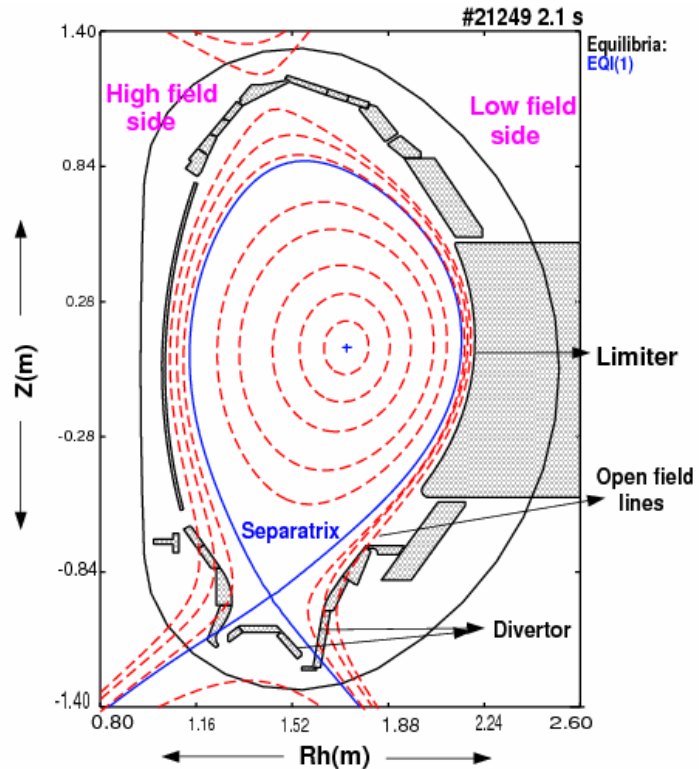


Fig.1. The Poloidal cross-section of the ASDEX Upgrade tokamak during equilibrium

Interestingly the impurity radiation contains information on the nature of the plasma and can be utilized to understand the plasma environment spectroscopically. However,

interpretation of spectroscopic measurements is not straight-forward. The delicacy lies in the complex nature of the tokamak plasma and subsequently the manifold atomic processes. In order to infer the plasma parameters from the measured intensities of lines, proper calculations of the population densities of excited states are sought.

In tokamak plasmas, many collisional and radiative processes may have non-negligible effects on the population distributions. So, in order to evaluate the population of excited states quantitatively an appropriate theoretical model and a large atomic database are required. The Collisional Radiative (CR) model that has evolved from pioneering work of Bates *et al.* [6] provides the theoretical basis for the calculation of the population density. At present there are a few CR-model based code -like ADAS [7-8], ALADDIN [9], and CHIANTI [10] etc used in the plasma physics community. The Atomic Data and Analysis Structure (ADAS) [8] package is an interconnected set of codes (which includes the CR model as well) and database for modeling the radiating properties of ions and atoms in the plasma. It covers most type of the atomic processes and the data required for fusion and laboratory plasma applications.

Moreover the performance of the divertor is essential for understanding how to optimize the main plasma parameters [11]. In fact, the divertor plasma isolates magnetically the strong plasma-wall interaction from the confined core plasma. This isolation helps in reducing the flux of recycled fuel particles and separated wall impurities back to the core plasma which finally assists in maintaining plasma density control and cleanliness of the plasma. The most noticeable achievement of divertor tokamak experiment is the production of H-mode (high confinement mode) plasma in the ASDEX [12] tokamak during high-power neutral beam injection which has led new generation tokamak experiments worldwide. The success of divertor tokamaks, such as JET, AUG, JT-60U and DIII-D is quite well known.

For future tokamaks, the divertor life time will become a critical issue due to the high power flux densities and in particular due to transient power loads caused by Edge Localized Modes (ELM's). The high heat flux is expected for ITER when it will be operational, which is challenging for divertor design and plasma facing components. Today's fusion research machines do not operate for long enough time (typically less than 8-10 minutes a day) and erosion has not been a significant problem. But when we eventually have a fusion reactor working long time (steady-state operation), erosion will be a big issue. Detached divertor plasmas, which have been studied for several years as a method to spread power deposition over larger area, have been found essential. In the detached divertor condition, the power load to the target in the boundary layer and in the divertor is reduced by radiation cooling, which leads to lower plasma temperature. These detached divertor plasmas are characterized by an increase in electron density and decrease in electron temperature such that plasma pressure and heat flux drops with increasing upstream density. This is typically accomplished by a strong increase of volume recombination [13-14]. However, since the underlying physics of detached and attached divertor plasma is still not fully understood, the divertor plasma is a region of actual research. To comprehend the divertor plasma parameters and plasma-wall interaction quantitatively, the detailed modeling with dedicated experimentation is necessary.

There are a wide variety of diagnostics equipped for these purposes in main plasma and divertor regions of the tokamak. Since spectroscopy relies on light being emitted from sources under investigation, it is a valuable technique. There are different ways in which light can be emitted from the plasma [15]. Radiation emitted from atoms and ions consists of individual spectral lines that contain information on the atomic level structure. The wavelengths of the lines are characteristic of the emitting species. Nevertheless, it is a general problem to record large wavelength range spectrum in a single snap shot avoiding errors introduced by shot to shot variation in spectroscopic analysis.

For quantitative understanding of divertor plasma parameters and for impurity influx measurements in ASDEX Upgrade, some dedicated shots have been taken using visible spectroscopy. The data have been collected for ohmic, H-mode and L-mode (low confinement mode) plasmas at three different locations i.e. midplane, outer and inner divertor of AUG using an ESA3000 Echelle spectrometer. This spectrometer allows simultaneous recording of the full visible and UV spectral range with high spectral resolution, albeit with low temporal resolution. The Stark broadening of deuterium Balmer series D_δ and D_γ lines are utilized to infer average electron density in the divertor region. A fitting procedure is developed to obtain these plasma densities using most recent Stark broadening tabulation code of Stehle *et al.* [16]. This code is based on Model Microfield Method [17] and also includes ion-dynamic effects. A probability analysis is carried out to derive self-consistent errors of the estimated densities. The plasma temperature, column densities of ground state atoms and ions are finally calculated using chi-square minimization procedure and full CR-model. This analysis provides the uncertainties of these measurements. A couple of boron and helium line pairs are identified which can be utilized to derive the effective electron plasma temperatures using line ratio technique [18]. The impurity influx measurements are then carried out using the ADAS atomic database at these estimated temperatures and densities. The measurements are compared with other diagnostics for consistency check.

Observation of attached and detached plasmas in ASDEX Upgrade during ohmic discharges is also reported. About 2 eV electron plasma temperature — calculated in the vicinity of the outer divertor — detached plasmas are observed. Under detached divertor conditions, the plasma temperature has dropped from 7-10 eV to \sim 2 eV in the outer divertor region. For increasing upstream density the deuterium flux increases significantly whereas carbon and boron fluxes reduce considerably. The existence of carbon flux, even in spite of very low temperature, may be due to the chemical sputtering instead of physical sputtering. Under detached divertor conditions the power flowing out of the core plasma disperses through radiation and neutrals to the wall rather than being conducted into a relatively smaller area on the divertor plates [19]. Eventually, the power delivered to the divertor plate should have reduced by the enhanced radiations to the wall that recycled the neutrals in the emission region and plasma can no longer be efficiently ionized.

The experimental setup used for this study is briefly explained in the section 2. The results and analysis are presented in the section 3. Section 4 contains information about the discussion, and conclusions are presented in section 5.

2. Experimental setup:

2.1 Operational regimes and heating systems:

The typical plasma parameters of the ASDEX Upgrade for the experiment herein were a discharge length of around 2-7 sec, 1 MA of plasma current and central plasma density was kept between $1 \times 10^{19} - 1 \times 10^{20} \text{ m}^{-3}$. A few shots (used in this study) and their working parameters are specified in the following table.

Table: I. Main plasma shots and their working parameters.

(Abbreviations: P_OH_Total: total ohmic power, Ipa_MAG: Plasma Current, PNI: Neutral beam injection power, PICRF: Ion-cyclotron resonance heating power. DCN_H-1: Average central electron density, DCN_H-5: Average edge electron density, B_t: Toroidal magnetic field. VOL2: Outer Lower Divertor, VIU2: Inner Upper Divertor, TOR-ROT: Mid plain line of sight)

Operational regimes	Shot. No AUG	Echelle Measurement Time (sec) [Used in this study]	Port	Ipa_MAG (MA)	Heating system/Power (MW)			Avg. N _e Center DCN_H-1 (m ⁻³)	Avg. N _e Edge DCN_H-5 (m ⁻³)	B _t (T)
					P_OH_TOT					
Ohmic discharges	21258	2.21-2.31	VOL2	0.8	0.73			3.6e+19	2.6e+19	-1.43
	21279	2.20-2.30	VOL2	1.0	1.11			2.6e+19	1.6e+19	-1.94
	21306	2.25-2.35	VOL2	1.0	0.94			3.9e+19	2.6e+19	-1.94
	21320	2.20-2.30	VOL2	1.0	0.88			3.9e+19	2.5e+19	-1.94
	21321	2.17-2.27	VOL2	1.0	1.18			5.0e+19	3.5e+19	-1.94
	21322	2.23-2.33	VOL2	1.0	1.53			6.5e+19	4.7e+19	-1.94
	21325	2.27-2.37	VOL2	1.0	1.06			4.8e+19	3.4e+19	-1.94
	21327	2.16-2.26	VOL2	1.0	1.28			5.0e+19	3.6e+19	-1.94
L-mode	21303	2.19-2.29	VOL2	1.033	0.668			2.6e+19	1.5e+19	-1.94
					PNI_NIS	PICRFc_ICP	P_OH			
H-mode (Edge modeling)	21249	2.25-2.35	VOL2	0.8	5.04	NIL	0.15	6.2e+19	4.4e+19	-1.93
	21250	2.23-2.33	VIU2	0.8	5.03	NIL	0.11	6.2e+19	4.4e+19	-1.93
	21252	2.19-2.29	TOR-ROT	0.8	5.04	NIL	0.14	6.2e+19	4.4e+19	-1.93
H-mode (NTM stabilization in improved H-mode)	21269	2.22-2.34	VOL2	1.2	5.05	1.04	2.34	7.4e+19	5.6e+19	-1.86
	21270	2.19-2.29	VIU2	1.2	5.05	2.76	0.45	6.5e+19	5.0e+19	-1.92
H-mode (divertor modeling)	21314	2.20-2.30	VOL2	1.0	5.03	1.90	0.35	8.4e+19	6.0e+19	-1.93
H-mode (ELM Ext. divertor Modeling)	21275	2.18-2.28	VOL2	0.8	5.03	NIL	0.22	5.4e+19	3.5e+19	-1.94
	21278	2.25-2.35	VOL2	0.8	6.55	NIL	0.14	5.3e+19	3.6e+19	-2.93
	21292	2.20-2.30	VOL2	0.8	6.56	NIL	0.15	5.2e+19	3.6e+19	-2.92
	21297	2.21-2.31	VOL2	1.0	5.03	NIL	0.39	7.3e+19	4.8e+19	-1.93
	21299	2.24-2.34	VOL2	1.0	5.04	NIL	0.66	8.9e+19	5.0e+19	-1.94
	21300	2.21-2.31	VOL2	1.0	5.03	NIL	0.31	7.2e+19	4.9e+19	-2.93
	21301	2.21-2.31	VOL2	1.0	5.03	NIL	0.35	9.5e+19	6.2e+19	-1.93
	21302	2.18-2.28	VOL2	1.0	6.55	NIL	0.39	8.2e+19	5.8e+19	-2.93
21304	2.24-2.34	VIU2	1.0	7.55	NIL	0.21	8.9e+19	5.9e+19	-1.93	

A typical plasma shot is shown in Fig.2. Experiments have been performed for three different regimes of operations, ohmic, H-mode and L-mode discharges. The flexibility in the heating systems mainly allows for various regimes of operations.

The heating systems available for ASDEX Upgrade are:

- (1). Neutral beam injection (NBI): The available heating power is ~ 20 MW.
- (2). Electron cyclotron resonance heating (ECRH) and ion cyclotron resonance heating (ICRH): The available heating power is ~ 2 MW (140 GHz) and 6 MW (30 MHz - 40 MHz) respectively.

In ohmic discharges the induced plasma current leads to the ohmic heating. However, since the resistivity of the plasma decreases with temperature, the ohmic power for heating is rather limited (~ 1 MW).

Operations with additional power, under certain conditions, has shown enhancement in the confinement above a power threshold. This regime of operation has been termed as the high-confined mode (H-mode) with transport barriers for energy and particles at the edge of the plasma [12]. In fact, in the magnetically confined plasmas, the small scale turbulences cause a radial particle and energy transport. Suppression of these turbulences is possible during the transport barrier formation which decreases radial diffusivity in a restricted plasma volume. In ASDEX Upgrade, with divertor configuration, the H-mode plasma is usually achieved with an appearance of few cm wide transport barrier near the separatrix. The confinement mode obtained below the power threshold is known as L-mode (for low-confinement). The achievable different modes can be sketched as shown in the Fig. 3 [20].

In stationary H-mode discharges the situation is not calm at the edge because very steep plasma pressure gradients at the edge lead to specific instabilities in the H mode, which is known as ELMs (for Edge Localized Modes) [21]. The plasma pressure profile relaxes

the situation is not calm at the edge because very steep plasma pressure gradients at the edge lead to specific instabilities in the H mode, which is known as ELMs (for Edge Localized Modes) [21]. The plasma pressure profile relaxes

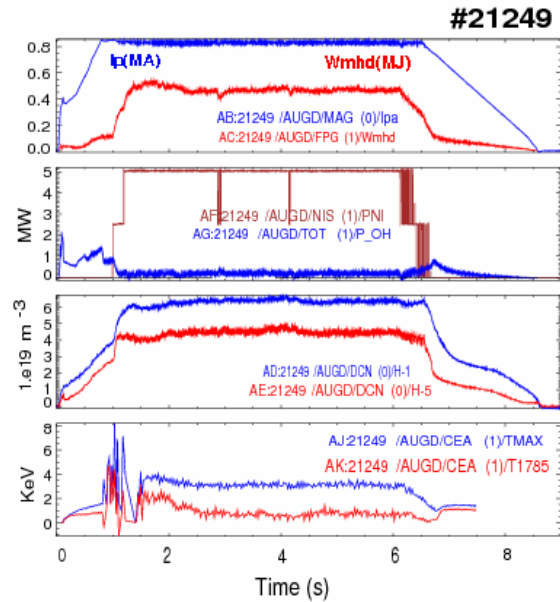


Fig.2. Time history of (i) current and stored energy, (ii) plasma heating power, (iii) central and edge average densities, (iv) electron temperatures for AUG #21249 at $q_{95} = 4.397$ and $B_t = -1.94$ T

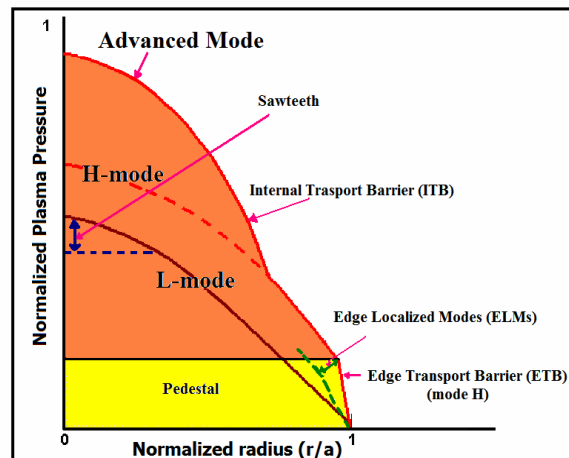


Fig.3. Schematic diagram of achievable plasma modes [20]

periodically towards less steep slopes as drawn in the Fig. 3 by green dotted line under the red curve. Then the barrier rebuilds itself, the profile steepens again before collapsing at the following ELM. Consequently, large particle and heat flux escapes from the plasma and can be deposited outside the separatrix at each ELM, imposing strong constraints on the wall and the divertor components.

The type-I ELMs occurs typically for H-modes in a frequency range of 2 to 100 Hz in ASDEX Upgrade. The type-III ELMs are smaller and more frequent than type-I ELMs. The type-II ELMs occur with a frequency in the range from 5 to 100 kHz at the plasma edge [22].

2.2 Spectrometer:

For simultaneous detection of multiple lines over a large spectral range, an Echelle spectrometer is the system of choice. It offers necessary spectral coverage and spectral resolving power. An Echelle spectrograph makes use of two dispersing elements, an echelle grating and a prism which is orthogonally placed. The echelle grating provides higher dispersion and higher resolution than a common echellete grating of the same size [23].

The blaze angle of an echelle grating is typically 63° - 76° significantly larger than conventional one (i.e., 10° - 38°) to achieve a high angle of incidence [23]. Also, the short side of the blaze is used rather than the long side to work in high reflection order. The gratings have typically 300 or less grooves per millimeter for UV/Visible radiation. The angle of refraction r is much higher in the echelle grating and approaches the angle of incidence i ($i \approx r$). Under these circumstances the condition for a constructive interference becomes,

$$2d \sin i = n\lambda, \quad (1)$$

where d signifies groove width, n order of diffraction and λ as wavelength.

Using a normal echellete grating high dispersion is obtained by making the focal length f

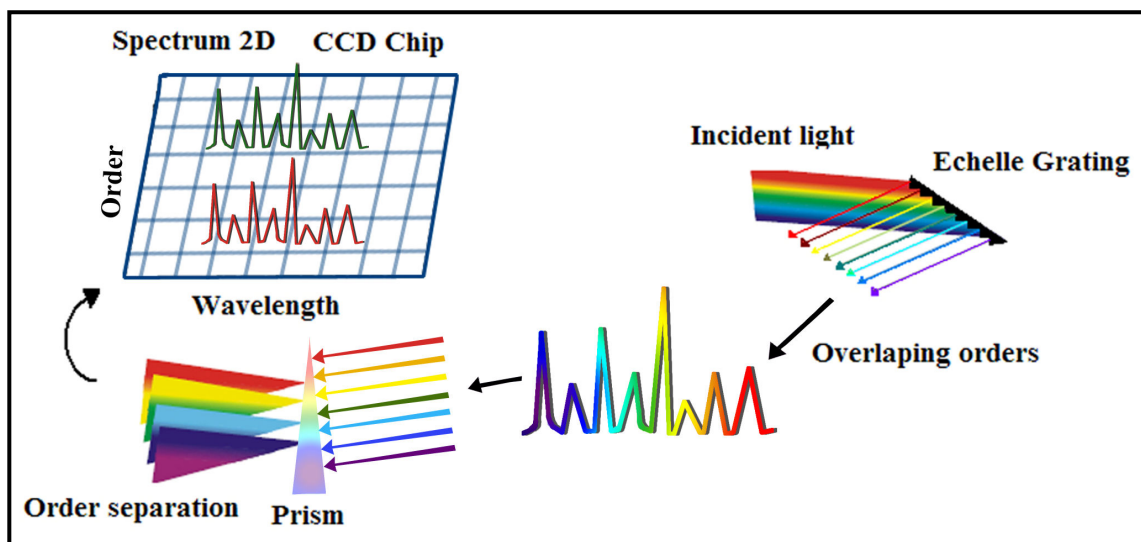


Fig.4. Schematic diagram of an Echelle spectrometer showing its basic principle

large and the groove width d small [23]. A large focal length degrades light gathering and leads to the larger dimensions of monochromators. On the other hand, the echelle grating achieves high dispersion by making both the angle i and the order of diffraction n large. The dispersion for an echelle grating is given by;

$$D = \frac{nf}{2d \cos i} \quad (2)$$

To cover a reasonably broad spectral range it is essential to use many successive orders and, due to this reason, the linear dispersion at the higher orders of refraction for an echelle grating is always extended. As these orders unavoidably overlap, it is necessary that another dispersing element is added. This is usually an orthogonally placed low-dispersion prism. A two dimensional spectrum can be generated by this method as sketched in Fig. 4. The spectral resolution achieved with the ESA3000 spectrometer is typically 0.028 nm-0.040 nm from lower to higher wavelength range. The orders are set between 30 and 120 for full wavelength coverage from 200 nm to 780 nm.

2.2.1 Detector:

The detector is an image-intensified charge coupled device (ICCD) with a wedge and strip readout system. A charge coupled device (CCD) camera system is equipped with an intensifier microchannel plate (MCP) which allows high photonics gain (about 10^6 electrons/photons) and possibility of electronic gating which is of importance for time resolved measurements. The available CCD chip consisted of 1024x1024 pixels. The more detailed information about principles and applications of CCDs and ICCD's can be found elsewhere [24, 25]. The actual spectrum taken by ICCD based ESA3000 echelle spectrometer between wavelength range 300 to 780 nm and orders between 31 to 81 is shown in Fig. 5.

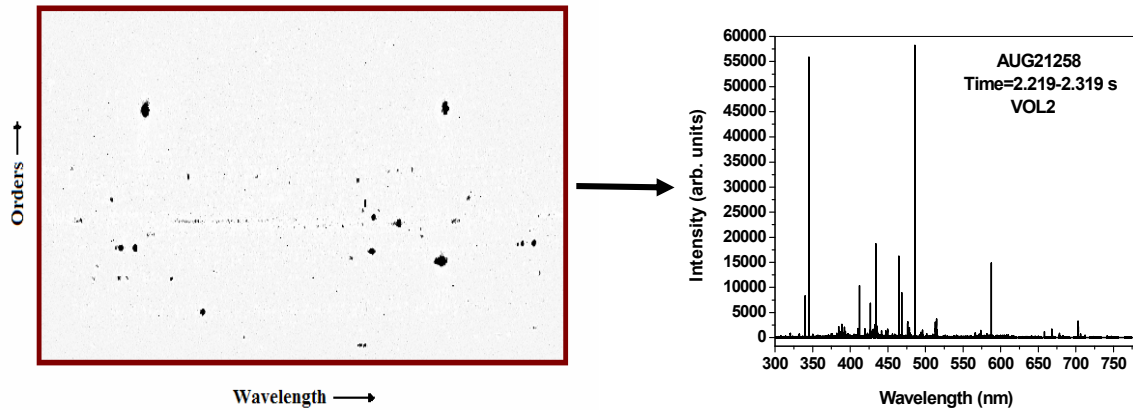


Fig.5. A typical spectra obtained by an ESA3000 Echelle spectrometer

The spectrum is recorded for 100 ms exposure time. After receiving a trigger pulse from ASDEX Upgrade, the external trigger unit is activated which generates an 80 ms pulse for the spectrometer at the fixed start delay of 100 ms. Now, to get correct exposure time corresponding to the experiment clock, 180 ms time has to be added in the recorded time of the trigger from the trigger unit. The rest of the time in between two recorded times

from the trigger unit is the readout time. The larger the wavelength range, the longer is the readout time. For full wavelength coverage from 200 nm to 780 nm, the readout time is approximately 4 sec. The set trigger parameters are,

Start delay = 100 msec, Time out = 5 sec,
Pulse width = 80 msec, Pulse level = 6.4 V
and Measurement mode = Local mode.

The light emitted from the plasma is fed to the spectrometer through optical fiber ca 50 m in length. Initially, the fiber cable is passing inside the vessel. It is then coupled to the fibers outside the vessel which ends up at a fiber switching table that allows easy selection of line-of-sight for the vessel to monitor. The two different line-of-sights for inner and outer divertor and their R, z and S coordinates are shown in Fig 6 and also listed below in table II. This table includes R, z and ρ_p values for midplane line-of-sight also.

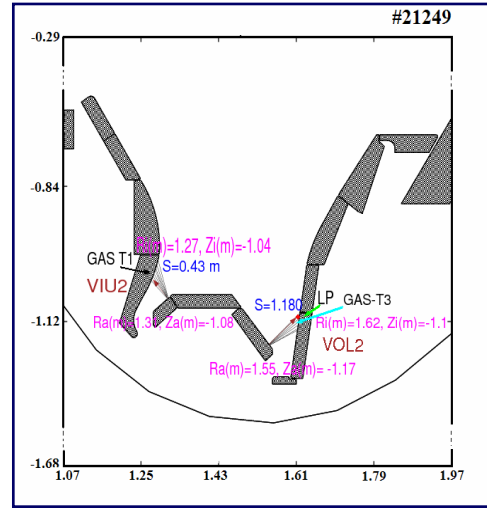


Fig.6. A schematic diagram for divertor line-of-sights and their viewing geometries

Table: II Table for lines-of-sights

Position	Ra (m)	phi-a	Za(m)	Ri(m)	Phi-i	Zi(m)	S-i
VOL2	1.55	0.0	-1.17	1.62	0.0	-1.1	1.18
VIU2	1.31	0.0	-1.08	1.27	0.0	-1.04	0.43
							ρ_D
TOR-MID	2.3347	0.0	0.47	2.1995	-31.5	0.2243	0.945

2.2.2 Calibration:

For quantitative analysis the calibration of a diagnostic is important. For spectroscopy, calibration in terms of absolute intensity and wavelength are required.

The wavelength calibration was already done previously. However, a first hand check was carried out and wavelength calibration is obtained by comparing a large number of deuterium, hydrogen, helium and boron lines recorded in the spectrum with the listed wavelengths in the NIST database [26]. A couple of deuterium and boron lines used for wavelength calibration are shown in Fig. 7. The found wavelength shift is around 0.01 nm positive.

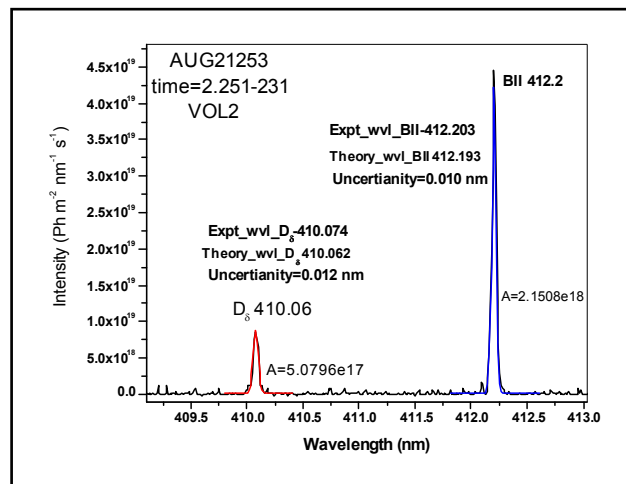


Fig.7. A comparison of the spectrum observed by ESA3000 Echelle spectrometer with NIST database

The Echelle spectrometer was absolutely calibrated beforehand in terms of intensity. A calibration curve was achieved for all intensified pixels at each of a set of wavelength settings which covers the measurement of wavelengths from 300 nm to 780 nm as shown in the Fig. 8. The curve obtained for each wavelength setting was kept separated and not combined into a single smooth sensitivity curve so that to preserve the calibration information of the individual pixels.

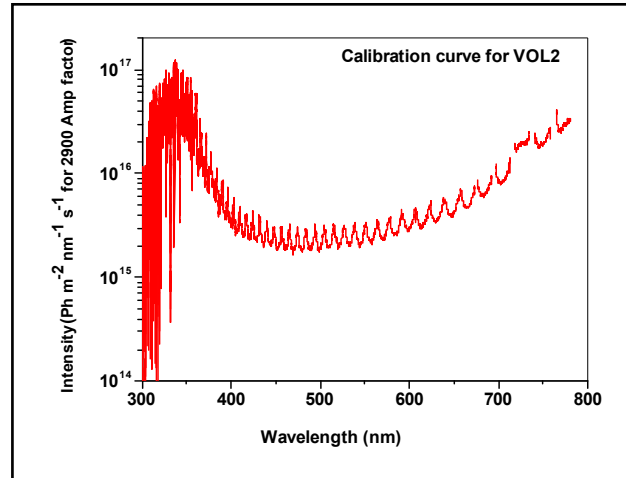


Fig.8. Absolute intensity calibration curve at each wavelength setting of ESA3000 Echelle spectrometer

2.3 Other Diagnostics:

(i). Lithium beam diagnostic for electron density measurements in the midplane at separatrix, (ii) Thomson scattering for electron temperature measurements in the midplane at separatrix, (iii) Langmuir probes (with probe area = $1.25 \times 10^{-4} \text{ m}^2$) for ion flux measurements near the two lines of sight with S-coordinates 1.178 m for VOL2 and 0.43 m for VIU2 respectively. The details of these diagnostics can be found in previous references [27-29].

3. Results and analysis:

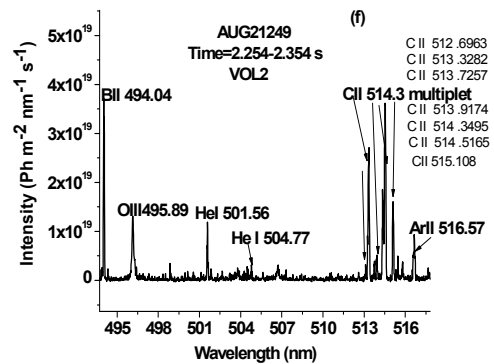
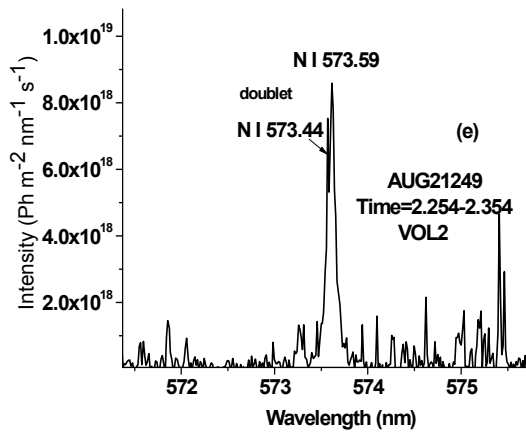
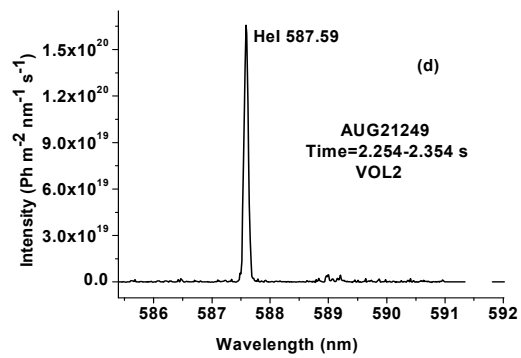
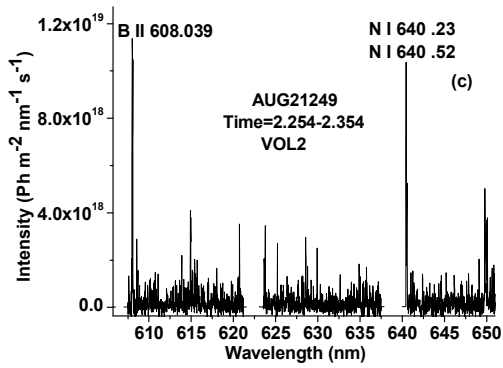
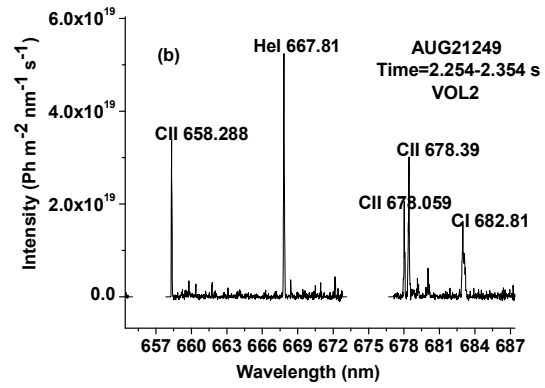
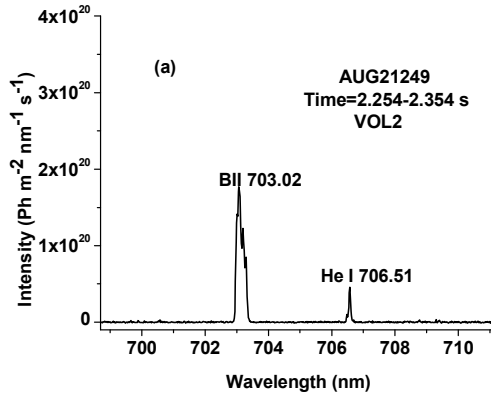
Observed lines in the spectral scan are identified using NIST [26] and ADAS [8] data tables with a preliminary knowledge of what impurity species are likely to be present for used vessel compositions. The relative strengths of certain identified lines are compared by plotting overlay synthetic spectrum using STRAHL code [30, 31] above the observed spectrum for exact wavelength identification. Table III shows the identified species (and their transitions) observed in the outer divertor region for H-mode plasma as an example. Spectral lines belonging to the deuterium Balmer series from D_β to D_ϵ are observed. The D_α signal was masked by the camera to avoid inconvenient saturation in the intensity signal which has helped in measuring low intensity spectral lines including molecular bands.

Table III: Identified spectral lines and their transitions in a shot # AUG21249 for H-mode plasma

Specie	Transition	λ_{th} (nm) from NIST, ADAS & ALADDIN databases	λ_{exp} (nm)	Comment
H I (β)	$4d - 2p$	4 86.13	486.15	deuterium and Hydrogen lines are indistingu- ishable
H I (γ)	$5d - 2p$	4 34.04	433.93*	
H I (δ)	$6d - 2p$	4 10.17	410.08*	
H I (ϵ)	$7d - 2p$	3 97.00	396.90*	
D I (β)	$4d - 2p$	486.00	486.01	
D I (γ)	$5d - 2p$	433.92	433.93*	
D I (δ)	$6d - 2p$	410.06	410.08*	
D I (ϵ)	$7d - 2p$	396.89	396.90*	
B II	$1s^2 2s 3p \ ^3P^o_2 - 1s^2 2s 3s \ ^3S_1$	703.02	703.06	Triplet
B II	$1s^2 2s 3p \ ^3P^o_1 - 1s^2 2s 3s \ ^3S_1$	703.20	703.21	
B II	$1s^2 2s 3p \ ^3P^o_0 - 1s^2 2s 3s \ ^3S_1$	703.23	703.28	
B II	$1s^2 2s 3p \ ^1P^o_1 - 1s^2 2p^2 \ ^1S_0$	608.039	608.05	Triplet
B II	$1s^2 2s 4f \ ^1F^o_3 - 1s^2 2s 3d \ ^1D_2$	494.04	494.05	
B II	$1s^2 2s 4p \ ^3P^o_2 - 1s^2 2s 3d \ ^3D^1$	478.42	478.43	
B II	$1s^2 2s 4s \ ^3S_1 - 1s^2 2s 3p \ ^3P^o_0$	447.20	447.20	
B II	$1s^2 2s 4s \ ^3S_1 - 1s^2 2s 3p \ ^3P^o_1$	447.21	447.25	
B II	$1s^2 2s 4s \ ^3S_1 - 1s^2 2s 3p \ ^3P^o_2$	447.28	447.29	
B II	$1s^2 2s 4s \ ^1S_0 - 1s^2 2s 3p \ ^1P^o_1$	419.48	419.49	
B II	$1s^2 2s 4f \ ^3F^o_4 - 1s^2 2s 3d \ ^3D_3$	412.19	412.20	
B III	$1s^2 5g \ ^2G - 1s^2 4f \ ^2F^o_{5/2}$	449.42	449.74	
B III	$1s^2 5f \ ^2F^o_{7/2} - 1s^2 4d \ ^2D_{5/2}$	448.71	448.76	
B III	$1s^2 5d \ ^2D_{3/2} - 1s^2 4p \ ^2P^o_{1/2}$	424.29	424.38	
He I	$1s 3s \ ^1S_0 - 1s 2p \ ^1P^o_1$	728.13	----->	
He I	$1s 3s \ ^3S_1 - 1s 2p \ ^3P^o_0$	706.57	706.56	
He I	$1s 3d \ ^1D_2 - 1s 2p \ ^1P^o_1$	667.81	667.83	
He I	$1s 3d \ ^3D_1 - 1s 2p \ ^3P^o_1$	587.56	587.58	
He I	$1s 3p \ ^1P^o_1 - 1s 2s \ ^1S_0$	501.56	501.67	
He I	$1s 4d \ ^1D_2 - 1s 2p \ ^1P^o_1$	492.19	492.21	
He I	$1s 4s \ ^3S_1 - 1s 2p \ ^3P^o_1$	471.31	471.32	
He I	$1s 3p \ ^3P^o_2 - 1s 2s \ ^3S_1$	388.86	388.87	
He II	4-3	468.57	468.58	
CI	$2s^2 2p \ (^2P^o) 4d \ ^1P_1 - 2s^2 2p \ (^2P^o) 3p \ ^1D^o_2$	682.81	682.93	Not clear
CII	$2s 2p \ (^3P^o) 3p \ ^4D_{3/2} - 2s 2p \ (^3P^o) 3s \ ^4P^o_{1/2}$	678.05	678.05	
CII	$2s 2p \ (^3P^o) 3p \ ^4D_{7/2} - 2s 2p \ (^3P^o) 3s \ ^4P^o_{5/2}$	678.39	678.41	
CII	$2s 2p \ (^3P^o) 3p \ ^4D_{5/2} - 2s 2p \ (^3P^o) 3s \ ^4P^o_{5/2}$	680.06	680.05	Triplet
CII	$2s^2 3p \ ^2P^o_{1/2} - 2s^2 3s \ ^2S_{1/2}$	658.28	658.32	
CII	$2s 2p \ (^3P^o) 3p \ ^4P_{3/2} - 2s 2p \ (^3P^o) 3s \ ^4P^o_{1/2}$	513.29	513.26	
CII	$2s 2p \ (^3P^o) 3p \ ^4P_{5/2} - 2s 2p \ (^3P^o) 3s \ ^4P^o_{3/2}$	513.32	513.34	
CII	$2s 2p \ (^3P^o) 3p \ ^4P_{1/2} - 2s 2p \ (^3P^o) 3s \ ^4P^o_{1/2}$	513.72	513.75	
CII	$2s 2p \ (^3P^o) 3p \ ^4P_{3/2} - 2s 2p \ (^3P^o) 3s \ ^4P^o_{3/2}$	513.91	513.93	
CII	$2s 2p \ (^3P^o) 3p \ ^4P_{3/2} - 2s 2p \ (^3P^o) 3s \ ^4P^o_{1/2}$	514.34	514.36	
CII	$2s 2p \ (^3P^o) 3p \ ^4P_{5/2} - 2s 2p \ (^3P^o) 3s \ ^4P^o_{5/2}$	514.51	514.53	
CII	$2s 2p \ (^3P^o) 3p \ ^4P_{5/2} - 2s 2p \ (^3P^o) 3s \ ^4P^o_{3/2}$	515.109	515.11	
CII	$2s^2 4f \ ^2F^o_{7/2} - 2s^2 3d \ ^2D_{5/2}$	426.73	426.75	
CII	$2s 2p \ (^3P^o) 4s \ ^4P^o_{1/2} - 2s 2p \ (^3P^o) 3p \ ^4S_{3/2}$	402.11	402.48	

CII	$2s^2(1S)4s^2S_{1/2} - 2s^2(1S)3p^2P^{\circ}_{3/2}$	392.07	}	390.08	Doublet
CII	$2s^2(1S)4s^2S_{1/2} - 2s^2(1S)3p^2P^{\circ}_{1/2}$	391.89		391.90	
CIII	$2s(2S)3p^3P^{\circ}_2 - 2s(2S)3s^3S_1$	464.74	}	464.75	Triplet
CIII	$2s(2S)3p^3P^{\circ}_1 - 2s(2S)3s^3S_1$	465.02		465.03	
CIII	$2s(2S)3p^3P^{\circ}_0 - 2s(2S)3s^3S_1$	465.14		465.15	
CIII	$2s(2S)5f^3F^{\circ}_4 - 2p(2P^{\circ})3p^3D_3$	416.29		416.30	
CIII	$2s(2S)5g^1G_4 - 2s(2S)4f^1F^{\circ}_3$	418.69		418.70	
CIII	$2s(2S)5g^3G_5 - 2s(2S)4f^3F^{\circ}_4$	407.03	}	407.04	Triplet
CIII	$2s(2S)5g^3G_4 - 2s(2S)4f^3F^{\circ}_3$	406.89		406.90	
CIII	$2s(2S)5g^3G_3 - 2s(2S)4f^3F^{\circ}_2$	406.79		406.80	
OII	$2s^22p^2(1D)3p^2F^{\circ}_{5/2} - 2s^22p^2(1D)3s^2D_{3/2}$	459.61	}	459.66	Doublet
OII	$2s^22p^2(1D)3p^2F^{\circ}_{7/2} - 2s^22p^2(1D)3s^2D_{5/2}$	459.09		459.15	
OII	$2s^22p^2(1D)4d^2D_{5/2} - 2s^22p^2(1S)3p^2P^{\circ}_{3/2}$	455.77		455.94	
OII	$2s^22p^2(3P)3p^2D^{\circ}_{5/2} - 2s^22p^2(3P)3s^2P_{3/2}$	441.49	}	441.50	Doublet
OII	$2s^22p^2(3P)3p^2D^{\circ}_{3/2} - 2s^22p^2(3P)3s^2P_{1/2}$	441.70		441.71	
OII	$2s^22p^2(1D)3d^2G_{9/2} - 2s^22p^2(1D)3p^2F^{\circ}_{7/2}$	418.98	}	419.00	Doublet
OII	$2s^22p^2(1D)3d^2G_{7/2} - 2s^22p^2(1D)3p^2F^{\circ}_{5/2}$	418.54		418.56	
OII	$2s^22p^2(3P)3d^4F_{9/2} - 2s^22p^2(3P)3p^4D^{\circ}_{7/2}$	407.58	}	407.59	Doublet
OII	$2s^22p^2(3P)3d^4F_{7/2} - 2s^22p^2(3P)3p^4D^{\circ}_{5/2}$	407.21		407.22	
OII	$2s^22p^2(3P)3p^2P^{\circ}_{1/2} - 2s^22p^2(3P)3s^2P_{1/2}$	395.43		395.45	
OII	$2s^22p^2(1D)3p^2P^{\circ}_{3/2} - 2s^22p^2(1D)3s^2D_{5/2}$	391.19		391.21	
OII	$2s^22p^2(3P)3d^4P_{3/2} - 2s^22p^2(3P)3p^4D^{\circ}_{1/2}$	387.40		387.59	
OII	$2s^22p^2(3P)3d^4D_{3/2} - 2s^22p^2(3P)3p^4D^{\circ}_{3/2}$	385.11	}	385.17	Triplet
OII	$2s^22p^2(3P)3d^4D_{5/2} - 2s^22p^2(3P)3p^4D^{\circ}_{3/2}$	385.08		385.04	
OII	$2s^22p^2(3P)3d^4D_{1/2} - 2s^22p^2(3P)3p^4D^{\circ}_{1/2}$	384.78		387.72	
OII	$2s^22p^2(1D)4s^2D_{5/2} - 2s^22p^2(1D)3p^2P^{\circ}_{3/2}$	373.57		373.71	
OIII	$2s^22p(2P^{\circ})3p^1P_1 - 2s^22p(2P^{\circ})3s^1P^{\circ}_1$	559.22		559.23	
OIII	$2s^22p^21D_2 - 2s^22p^2^3P_1$	495.89		496.10	
OIII	$2s2p^2(4P)3d^3P_2 - 2s^22p(2P^{\circ})4d^3D^{\circ}_3$	476.17		476.30	
OIII	$2s^22p(2P^{\circ})3p^3D_2 - 2s^22p(2P^{\circ})3s^3P^{\circ}_1$	375.42	}	375.48	Triplet
OIII	$2s^22p(2P^{\circ})3p^3D_1 - 2s^22p(2P^{\circ})3s^3P^{\circ}_0$	375.72		375.73	
OIII	$2s^22p(2P^{\circ})3p^3D_3 - 2s^22p(2P^{\circ})3s^3P^{\circ}_2$	375.98		375.99	
OIII	$2s2p^2(4P)3d^3F_3 - 2s2p^2(4P)3p^3D^{\circ}_3$	374.69		374.94	
N I	$2s^22p^2(3P)4d^4D_{1/2} - 2s^22p^2(3P)3p^4D^{\circ}_{1/2}$	640.23	}	640.45	Doublet
N I	$2s^22p^2(3P)4d^4D_{5/2} - 2s^22p^2(3P)3p^4D^{\circ}_{3/2}$	640.52		640.55	
N I	$2s^22p^2(3P)5d^4D_{3/2} - 2s^22p^2(3P)3p^4P^{\circ}_{1/2}$	573.44	}	573.57	Doublet
N I	$2s^22p^2(3P)5d^4D_{1/2} - 2s^22p^2(3P)3p^4P^{\circ}_{1/2}$	573.59		573.61	
Ca I	$4s4p^1P^{\circ}_1 - 4s^21S_0$	422.67		422.68	Weak line
Ca II	$3p^6(1S)4p^2P^{\circ}_{3/2} - 3p^6(1S)4s^2S_{1/2}$	393.33		393.37	Weak line
Mo I		405.12		405.22	Weak line
Mo I		390.30		390.40	Weak line
Ar II		516.57		516.68	Not clear

The identified spectral lines indicate that the main impurities present in the plasma are Boron, Helium, Carbon and Oxygen with different ionizing stages. A few Nitrogen Molybdenum, Argon and Calcium lines are also present. The measured spectrum in one of the low density H-mode discharge (shot # AUG21249) with absolute intensity scale is shown in Fig. 9. The observed CD, BD 0-0, BD 1-1 molecular bands in the same shot are shown in Fig. 10.



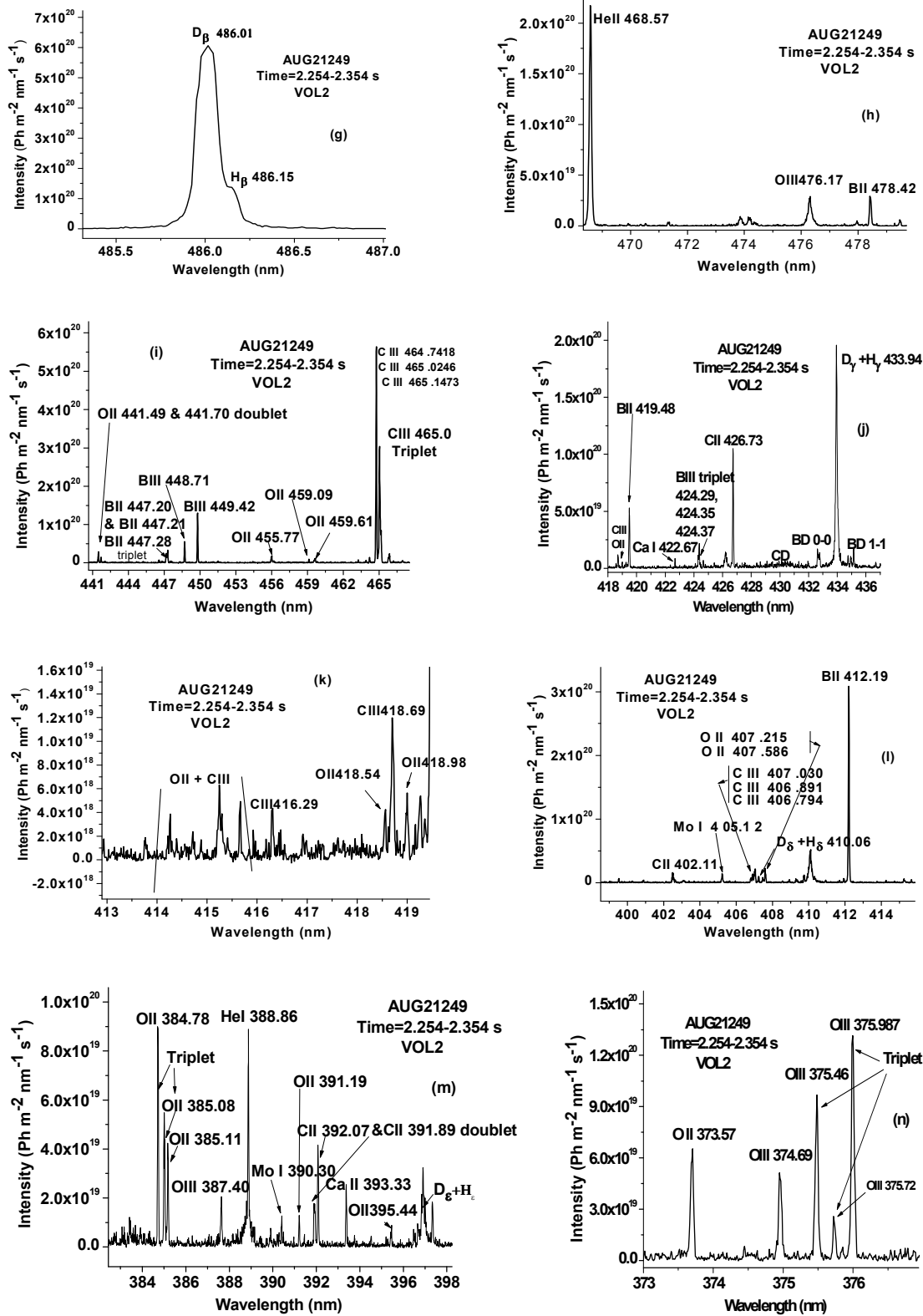


Fig.9. Typical plasma spectrum obtained for low density H-mode discharge (shot # AUG21249) (a)-(n)

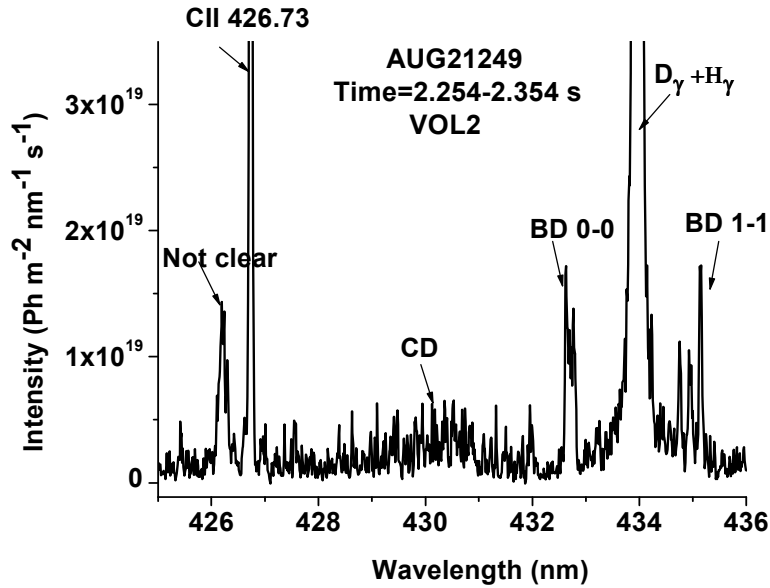


Fig.10. Spectrum with observed molecular bands

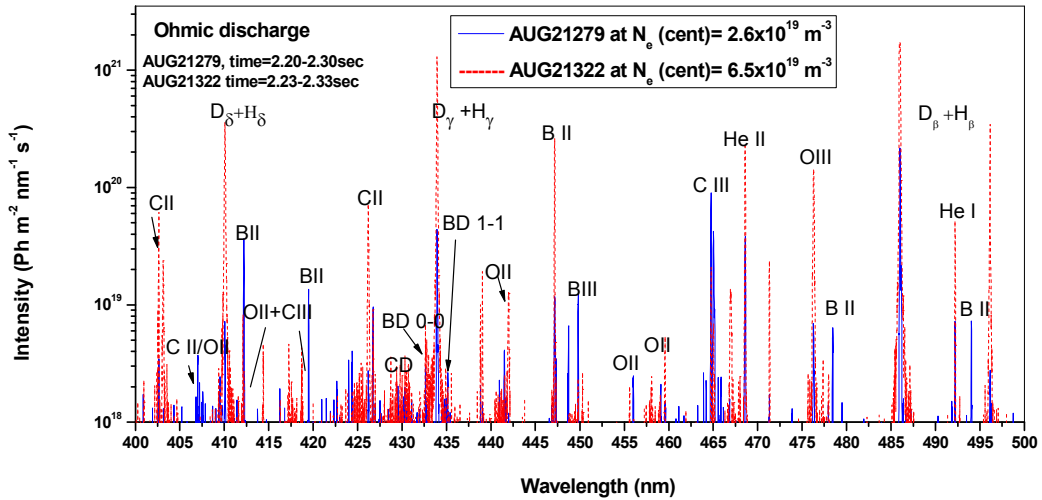


Fig.11. A comparison of the obtained spectra for low and high density plasma cases outer divertor region

A comparison of the obtained spectra for low and high density plasma cases has been made for ohmic discharges in the outer divertor region (see Fig. 11). The carbon and boron photon fluxes have reduced around one order of magnitude in the high density ohmic discharge. The deuterium fluxes have increased in the same order. The comparison of the spectra obtained in the outer divertor, inner divertor, and midplane for H-mode plasma at a fixed central density is shown in the Fig. 12. The photon fluxes

obtained in the inner divertor are much weaker relative to the outer divertor and midplane plasmas. At the same time midplane photon fluxes are also weak relative to the outer divertor plasma but stronger than the inner one. The very weak flux in the inner divertor qualitatively tells that the inner divertor is much cooler than the outer divertor in the low density H-mode discharges. For quantitative analysis in the inner divertor and midplane plasmas an absolute intensity calibration is required.

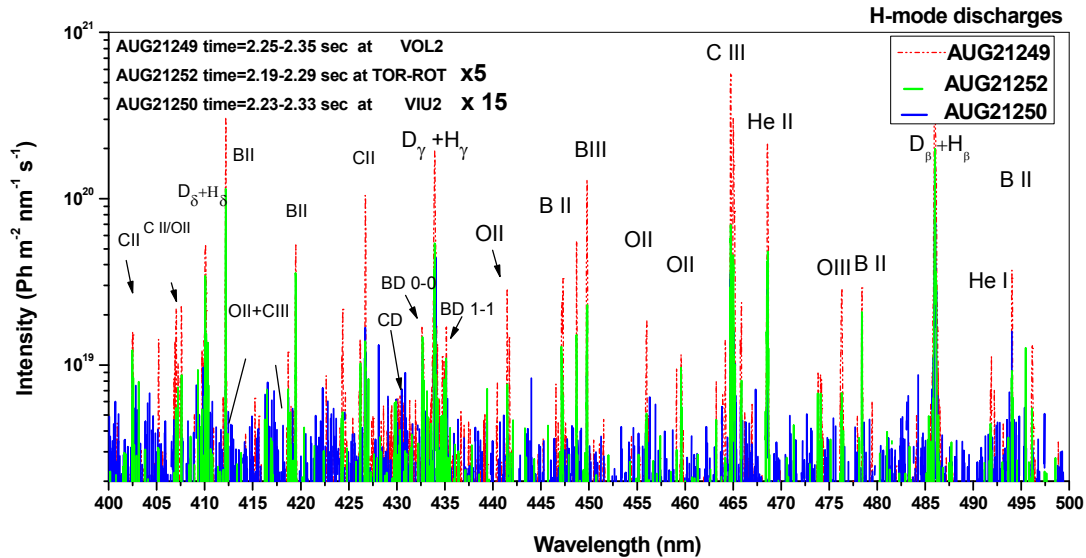


Fig.12. A comparison of the obtained spectra in the inner divertor, outer divertor and midplane plasmas during H-mode discharges for $\langle N_e \rangle_{CENT} = 6.2 \times 10^{19} \text{ m}^{-3}$.

3.1 Plasma Parameter Measurements:

3.1.1 Density measurements:

The spectral lines of hydrogen and hydrogenlike ions emitted from plasmas exhibit significant broadening compared to lines of other plasma constituents due to linear Stark effect. The shapes of these lines depend not only on the specific transition between two energy levels but also on the density of charged particles surrounding the emitting hydrogen atoms or hydrogenic ions. The Stark broadening of these lines is often applied for plasma diagnostic purposes. In particular the hydrogen lines of the Balmer series are frequently used as a measure of electron density in plasmas [32-36].

In conjunction with Vidal, Cooper and Smith (VCS) tables [37] the efforts have been made to determine electron density from the experimental H_β line width [38]. The overall agreement of the experimental H_β profile with VCS [37] was good except for the central part where the theoretical profile always has a larger dip. This discrepancy is related to the effect of ion-dynamics on the line shape. In order to overcome this problem and make use of other Balmer series lines, two recent theoretical calculations, one based computer simulation by Gigosos [39] and another on Model Microfield Method (MMM) by Stehle *at al* [16] are performed. It is established that the Stark broadening in H_β line is only useful for density diagnostics between $10^{22} - 10^{23} \text{ m}^{-3}$ and does not help in the regime of

our density interest [40]. Therefore, one has to look for the higher members of hydrogen Balmer lines. In this work we have used Balmer series D_δ and D_γ lines for plasma density measurement.

We have developed a numerical procedure for electron density determination by fitting experimental profile of deuterium (and hydrogen) Balmer series D_δ and D_γ lines with theoretical ones. Theoretical data are taken from broad tabulation code of Stehle [16]. This procedure enabled fitting of area or intensity normalized profile of deuterium Balmer series lines including the hydrogen admixture with the theoretical line profiles. To find the function which is the optimal fit to the data, we minimize chi-square (i.e. weighted sum of squares of deviations between the measurements and the predicted values) of profiles for these measurements at given sets of N_e and T_{eff} as guess values. The quantity N_e symbolizes for electron density and T_{eff} represents the effective temperature responsible for Doppler broadening solely caused by the thermal effect of background species and instrument broadening. The grid for N_e and T_{eff} is kept between 1×10^{18} - $1 \times 10^{21} \text{ m}^{-3}$ and 0.4-10.0 eV respectively. The chi-square values are greatly reduced for certain values of densities as shown in Fig. 13.

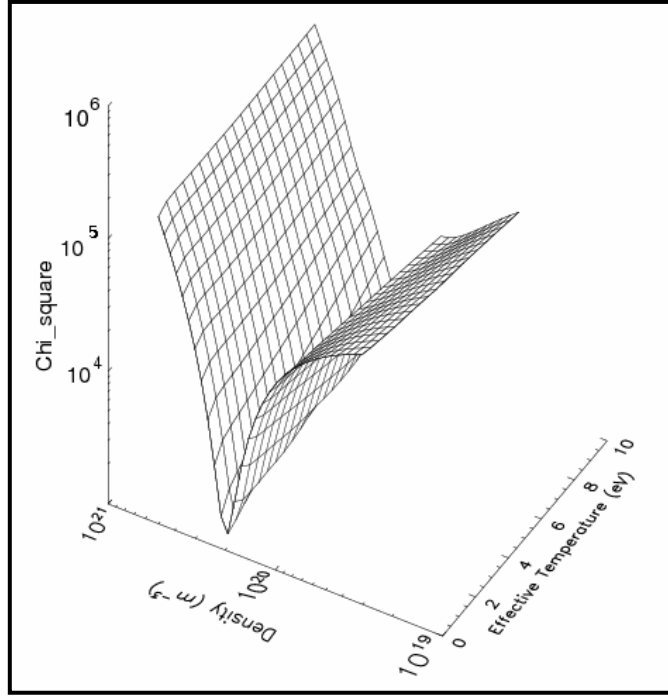


Fig.13. A chi-square map for ohmic discharge #21327

The fit which gives the smallest sum of squares (or the least-square fit) maximizes the probability for the measurements which comes from the parent distribution described by the fit. But how we will determine what parent distribution is given? The statistical mechanics have shown that the many small perturbation (errors) that affect a physical system almost always force the measurement to follow the Gaussian distribution. It is usually referred to as simply the “normal distribution”. Using the $\chi^2(T_{\text{effj}}, N_{\text{ek}})$ map of j number of effective temperatures and k number of densities and the normal distribution, the probability of observing the fit of k densities will be given by,

$$P < N_e >_k = \sum_j \exp\left(-\frac{1}{2} \tilde{\chi}^2(T_{\text{effj}}, N_{\text{ek}})\right) \quad (3)$$

where $\tilde{\chi}^2(T_{\text{ij}}, N_{\text{ek}}) = \chi^2 - \chi_{\text{min}}^2$ and χ_{min}^2 represents the minimum value of the chi-square on chi-square map. This scheme has averaged out the T_{eff} dependency on the experimental line profile. The obtained probability distribution function and the value of the density from the peak measurement of this distribution for a D_δ line are shown in Fig. 14 (a). The preliminary errors on these estimated densities are calculated from the full-

width-half-maxima (FWHM) of the probability distribution function. To avoid other systematic errors from this method a comparison of the density estimations obtained from the Stark broadening of the D_γ line is carried out. The D_γ line is equally interesting for density measurements except the noticeable influenced by molecular bands (see fig 10) which estimate somewhat higher density in comparison to D_δ line [see Fig. 14 (b)]. The cases where molecular spectra are not significant, the two density estimations match within 11 % (e.g., # 21327). We have adopted the density estimation from the Stark broadening of D_δ line (i.e., due to no influence) and relative errors are derived by comparing it with D_γ line. The obtained densities using the Stark profiles of D_δ and D_γ lines in # 21327 are $2.16 \times 10^{20} \text{ m}^{-3}$ and $2.39 \times 10^{20} \text{ m}^{-3}$ respectively. For # 21258 the values are highlighted in the figures blow.

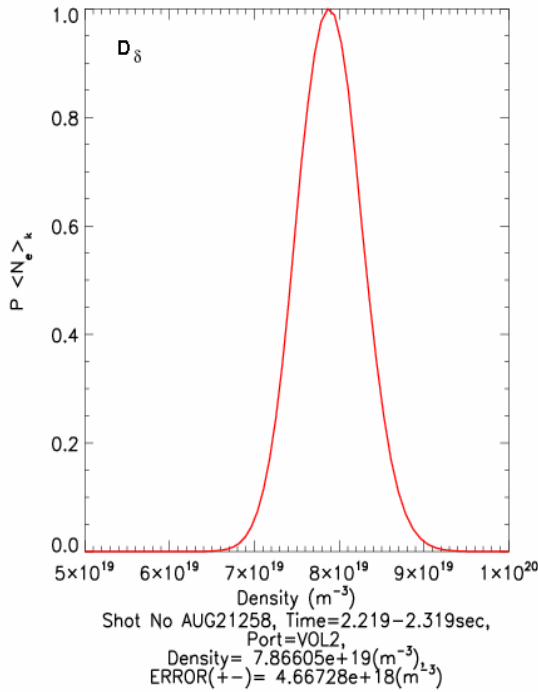


Fig.14.a. A curve for probability density distribution obtained for # 21258 using D_δ line

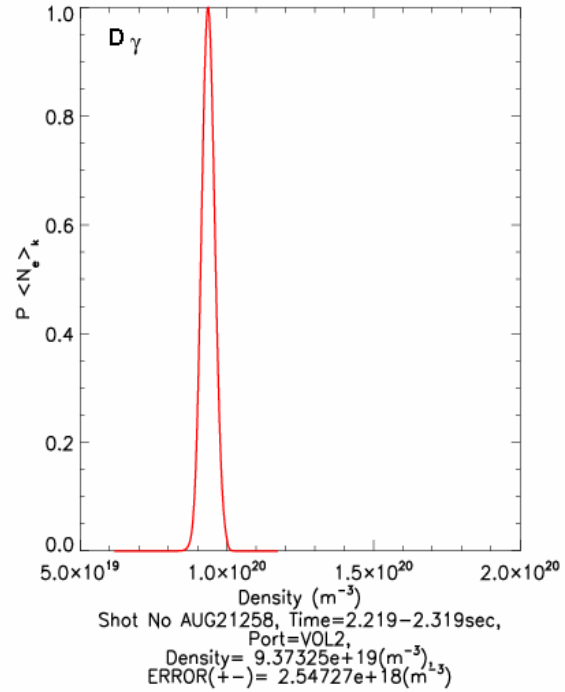


Fig.14.b. A curve for probability density distribution obtained for # 21258 using D_γ line

The Zeeman broadening has not been taken into account. It is to be noted that the Zeeman effect may only influences the central part of the line profile whereas the Stark effect is determined by the far wings of the line profile.

An alternate density measurement is also carried out using Voigt fit procedure from the observed experimental profile of D_δ line. The so-called Voigt profile is the spectral line shape which results due to the contributions from different broadenings of an emission line originating from a point in the plasma and is superposition of independent Lorentzian and Gaussian line broadening mechanism. To an extent people assume that the Lorentzian profile is same as the Stark profile and determine the density from measured Lorentzian width using Voigt fit procedure [41-42]. We have made a comparison that is elaborated in the discussion section. The proper convolution of different broadening with this method gives an additional check which supports averaging out the T_{eff} in the above analysis.

3.1.2. Temperature measurements (CR-model and Line ratio technique):

3.1.2.1 Hydrogenic Balmer lines:

The emissivity (photons $\text{m}^{-3} \text{sec}^{-1}$) of an optically thin spectral line of wavelength λ_{ul} due to a transition from upper level u to lower level l is given by,

$$\varepsilon_{\lambda_{ul}} = N_u A_{ul} \quad (4)$$

and its intensity $I(\lambda_{ul})$ is given by

$$I(\lambda_{ul}) = \frac{1}{4\pi} \int_{x_1}^{x_2} N_u A_{ul} dx \quad \text{photons m}^{-2} \text{s}^{-1} \text{sr}^{-1}, \quad (5)$$

when the plasma is viewed along a line of sight (LOS) that traverses the plasma from x_1 to x_2 . Here A_{ul} is the spontaneous transition probability from upper to lower level, N_u is the number density population of the upper level u of the emitting ion and x is the distance along the line of sight. With an assumption of average electron density and temperature in an emission length x , the photon intensity of a spectral line for such averaged measurement can be written from the CR-model as,

$$\tilde{I}(\lambda_{ul}) = \text{PEC}_{\text{recombining}} \tilde{N}_e(\tilde{N}_i x) + \text{PEC}_{\text{excitation}} \tilde{N}_e(\tilde{N}_g x) \quad (6)$$

where $\text{PEC}_{\text{recombining}}$ and $\text{PEC}_{\text{excitation}}$ represents the effective photon emission coefficients (photons $\text{m}^3 \text{sec}^{-1}$) for recombination and excitation processes in an average measurement. Here $\tilde{N}_g x$ and $\tilde{N}_i x$ are the average column densities of the ground state atoms and ions. The ADAS code derives PEC values for particular line λ_{ul} after calculating the population distribution of levels. This is done by solving a set of coupled rate equations for a number of levels of the ionization stage i . In each equation, one includes all the processes of populating and depopulating the level by excitation, de-excitation, spontaneous emission, ionization and recombination from adjacent ionization stages etc [8]. The effective emission coefficients are nonlinear functions of electron densities and temperatures. Understandably the measured average intensities are also complex functions of the electron density, electron temperature along with column densities of ground state atoms and ions. These are the quantities which one needs to know.

In order to derive these four unknowns we have to apply at least four such equations [i.e., eq(6)] from four different spectral lines of a particular species and deal with a model which depends nonlinearly on the set of unknown parameters. Different lines of deuterium Balmer series D_β , D_γ , D_δ , and D_ϵ are used for this purpose. The procedure is to define χ^2 merit function and determine best-fit parameters by its minimization. For given trial values for the parameters, we have employed a procedure that improves the trial solution. The procedure is repeated until χ^2 effectively stop decreasing to derive all the four unknown quantities and their estimated errors. The estimated values are tabulated below for couple of shots. The errors, based on our estimations, have been propagated in the code. The accounted errors are due to signal and photonic noises and also from the density estimation from the Stark broadening calculations. The calibration errors are not included. Further analysis is required for more robust measurements because in few shots χ^2 minimization has shown multiple minima which indeed demand more input data to be taken in the model and apparently more work to establish our premise.

Table IV: The details of estimated plasma parameters in the ohmic series discharges along with low-density H-mode discharge

Shot No.	T_e (eV)	error %	N_e (m^{-3})	error %	$\tilde{N}_g x$ (m^{-2})	error %	$\tilde{N}_i x$ (m^{-2})	error %
21258	7.87	10.8	7.86×10^{19}	13.6	3.03×10^{16}	10.6	4.54×10^{18}	150.0
21279	7.33	29.9	6.21×10^{19}	21.5	1.60×10^{16}	31.1	3.82×10^{18}	176.3
21320	10.3	21.5	7.72×10^{19}	21.6	1.43×10^{16}	24.1	1.20×10^{18}	Independent
21322	1.54	15.2	1.26×10^{20}	16.6	2.63×10^{19}	106.5	4.69×10^{18}	28.0
21325	1.62	8.9	2.06×10^{20}	14.9	1.73×10^{19}	57.2	2.87×10^{19}	23.2
21327	1.56	4.4	2.47×10^{20}	6.6	3.39×10^{19}	28.3	5.41×10^{19}	10.8
Low density H-mode								
21249	8.58	31.7	2.25×10^{20}	22.5				

The large errors in the values of $\tilde{N}_i x$ and $\tilde{N}_g x$ indicate that the absolute photon intensities depend poorly on one of these quantities. In equation (6), the population that is proportional to the ion density is the recombining component, and proportional to the ground state density is the ionizing component and depending on the dominance of one of these quantities plasma is termed as ionizing or recombining plasma from the CR-model [43]. For the above mentioned ohmic discharges the ionizing and recombining terms are obtained using D_γ line as listed below.

Table V: Obtained recombining and ionizing terms in the ohmic series discharges

Shot No.	$PEC_{recombining}$		Recombining term		$PEC_{excitation}$		Ionizing term	
	photons sec^{-1}	m^3	$PEC_{recombining}$	$\tilde{N}_e (\tilde{N}_i x)$	photons sec^{-1}	m^3	$PEC_{excitation}$	$\tilde{N}_e (\tilde{N}_g x)$
			Ph. $m^{-2} sec^{-1}$				Ph. $m^{-2} sec^{-1}$	
21258	1.01×10^{-21}		3.59×10^{17}		2.83×10^{-18}		6.74×10^{18}	
21279	1.13×10^{-21}		2.69×10^{17}		2.94×10^{-18}		2.92×10^{18}	
21320	6.64×10^{-22}		6.15×10^{16}		4.49×10^{-18}		4.96×10^{18}	
21322	1.51×10^{-20}		8.94×10^{19}		6.39×10^{-21}		2.12×10^{19}	
21325	1.39×10^{-20}		8.23×10^{19}		6.74×10^{-21}		2.40×10^{19}	
21327	1.49×10^{-20}		1.99×10^{20}		4.61×10^{-21}		3.86×10^{19}	

The first term of equation (6) is smaller than the second term for the first three shots whereas for next three it dominates second. It clearly specifies that the first three discharges satisfy the ionizing plasma condition and other three satisfies recombining plasma condition. A comparison of the obtained electron densities and temperatures for increasing upstream densities is shown in the Fig. 15. The ionizing and recombining plasmas are highlighted in the dotted box. In recombining plasmas the temperature has drop to ~ 2 eV from the 7-10 eV of the ionizing cases and also plasma pressure has reduced significantly. The recombining plasmas are

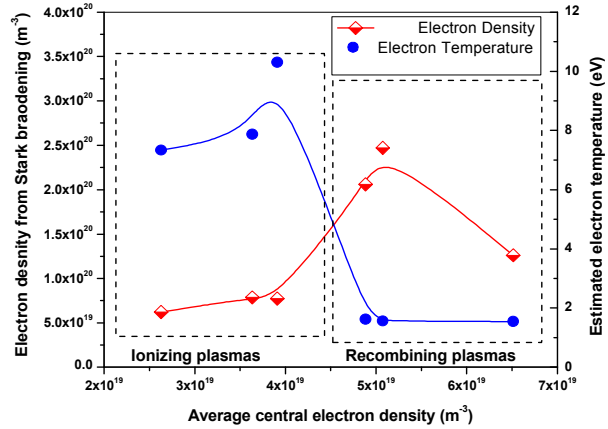


Fig.15. A comparison of the estimated electron densities and temperatures for increasing upstream densities

recombining plasmas the temperature has drop to ~ 2 eV from the 7-10 eV of the ionizing cases and also plasma pressure has reduced significantly. The recombining plasmas are

the indication for the detached divertor condition. More details are discussed in the subsequent subsections.

3.1.2.2 Impurity line ratios:

The ratios of two different lines of single species are also used as temperature or density diagnostics in plasmas. This procedure is applicable for the cases when the plasma is either purely ionizing or recombining. For example, in the ionizing plasma the equation

$$(6) \text{ reduces to } \frac{N_u A_{ul}}{N_i N_e} = \text{PEC}_{\text{excitation}} = (X_{ul})_{\text{eff}}$$

photons $\text{m}^3 \text{sec}^{-1}$. Since the effective emission coefficients are functions of electron density and temperature, the ratio of two lines cancels the leading $N_e N_i$ dependence in the ratio output.

The experimental observable intensity ratio of two lines can be easily obtained from the ADAS code as the ratio of corresponding emission coefficients and the diagnostic plot of ratios depending on temperature and density can be computed. The line ratios which are sensitive to one of the quantities (either temperature or density) and insensitive to other quantity have to be identified for this purpose. We have obtained certain useful line ratios which complement the obtained values of densities and temperatures from the full CR-model under ionizing condition. A couple of boron line ratios [i.e. B II 703.20 (triplet) / B II 419.48, B

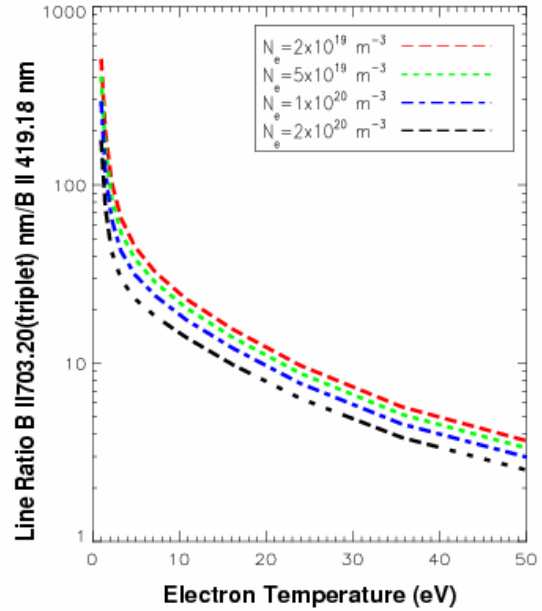


Fig.16(a). Absolute line intensity ratio of B II 703.20 (triplet) / B II 419.48

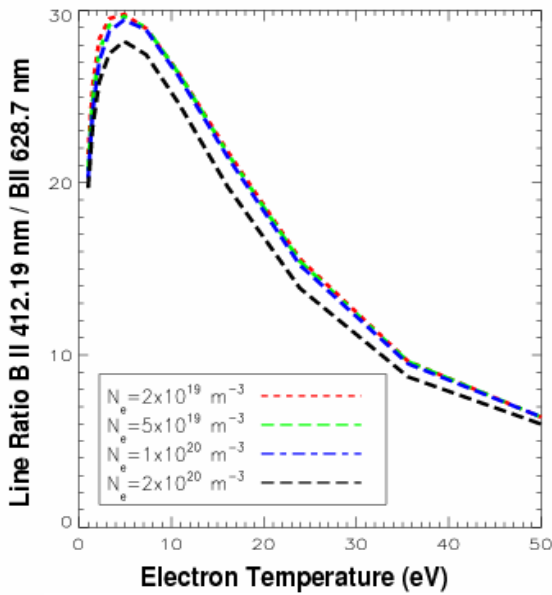


Fig.16(b). Absolute line intensity ratio of B II 412.19/ B II 628.7

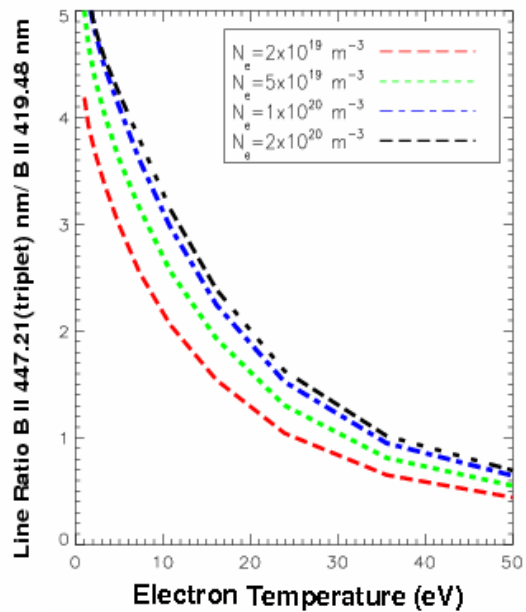


Fig.16(c). Absolute line intensity ratio of B II 447.21(triplet)/ B II 419.48

II 412.19/ B II 628.7 and B II 447.21(triplet)/ B II 419.48] are identified temperature sensitive, and shown in the Fig. 16. However, the absolute intensity of BII 419.48 reduced very much for increasing upstream density in the ohmic series discharges and BII 628.7 is not visible for our cases. In this condition, helium line ratio He I 667.8/ He I 706.57 can be utilized by feeding density as input from the Stark broadening calculations (see fig. 17) because this line ratio is quite sensitive to both density and temperature. A density sensitive line ratio is also obtained for hydrogen lines (H_{β}/H_{δ}) as shown in Fig. 18, which is quite applicable for density measurements in the unshaded region. For example in # 21258 the value of H_{β}/H_{δ} ratio is ~ 29 and can be fitted with this ratio.

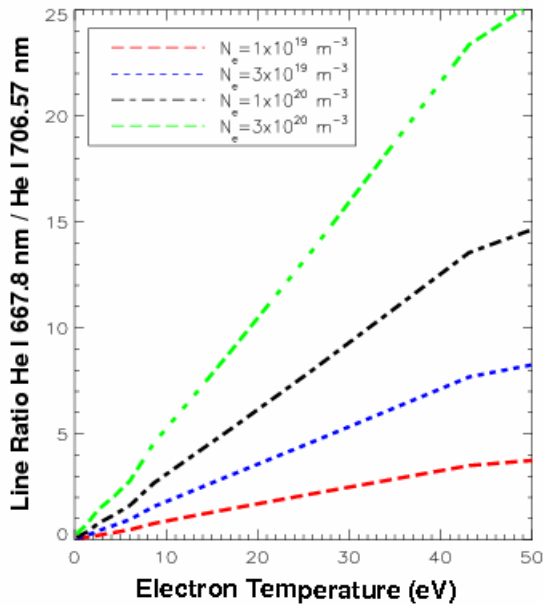


Fig.17. Absolute line intensity ratio of He I 667.8/ He I 706.57

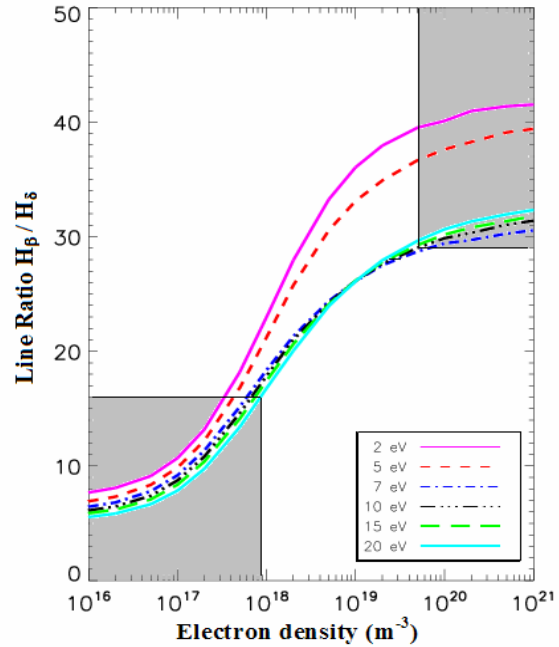


Fig.18. Absolute line intensity ratio of H_{β}/H_{δ}

With the above mentioned selection of line ratios, we made a comparison of the obtained experimental line ratios with the theoretically calculated ratios at the estimated temperature and density values from the full CR-model. The ratios of BII 703.20 (triplet) / B II419.48 and He I 667.8/ He I 706.57 are shown in Fig. 19. The experimental and theoretical line ratio matches well with the full CR calculations for the ionizing plasma except the discharge # 21320 where a strike point sweep possibly disturbed the measurements. The time averaged values of the difference between the strike point position and spectroscopic line-of-sight (LOS) is shown in the Fig. 20. Since we have made all average measurements, it could be a possible effect of strike point sweep that is invisible. Moreover for recombining plasmas the above line ratio fails. We find 3-3.5 eV electron temperature from the comparison of the observed experimental helium ratio and the above shown line ratio under ionizing condition for # 21322, # 21325 and #21327 which is higher than the full CR-model calculations. It is quite obvious because these ratios are merely derived under ionizing condition and interpretation of recombining plasmas by the ionizing ratio may mislead the results. Thus, in the recombining plasmas, full CR-model calculations are necessary otherwise suitable line ratios applicable for the recombining condition have to be found out.

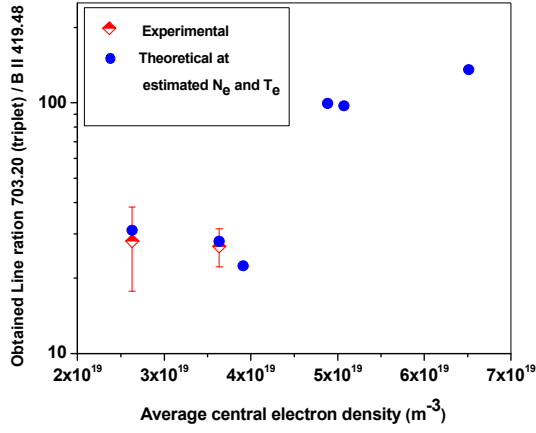


Fig.19(a) Theoretical and experimental line ratios of BII 703.20 (triplet) / B II419.48

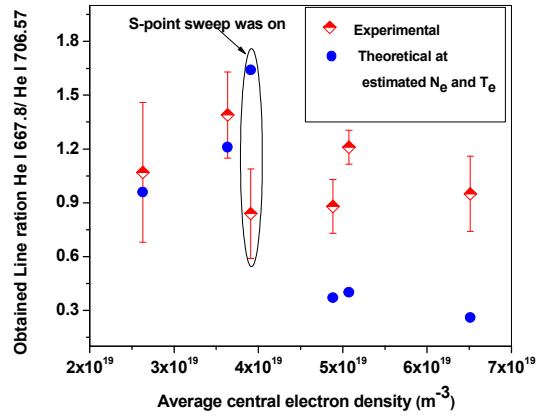


Fig.19(b) Theoretical and experimental line ratios of He I 667.8/ He I 706.57

3.2 Impurity influx measurements from outer divertor (S/XB Ratio technique):

At the plasma edge, where the plasma is in contact with a material surface, neutrals enter the plasma and are rapidly ionized, accompanied by radiation. The recombination is negligible if T_e is sufficiently high (ionizing plasma). By monitoring the intensity of a characteristic spectral line, the flux of atoms entering the plasma can be inferred. This requires knowledge of ionization coefficient S and the excitation coefficient X for the line monitored (along with the branching ratio B , which accounts for the fact that the upper level may also be radiating on other transitions apart from the one observed). The above calculations are well-known [8, 44] and are simply expressed as,

$$\Gamma_i = \frac{S}{XB} I_{total}, \quad (7)$$

where the S/XB ratio coefficient is the reciprocal of the photon efficiency coefficient which relates the emission of the spectrum line intensity I_{total} , to the neutral particle flux Γ from the surface. The validity of the computed S/XB ratio (and hence the accuracy of the inferred flux) depends on the atomic processes correctly taken into account and the available atomic physical data for these processes. The ADAS package contains such data and has been utilized to investigate the impurity influxes.

To understand the impurity behavior in the outer divertor region, the exact S/XB values are obtained at the estimated values of temperatures and densities for the observed different species. The fluxes for number of spectral lines of a single ionizing stage are summed up and mean values are taken to bring out more useful results. The impurity

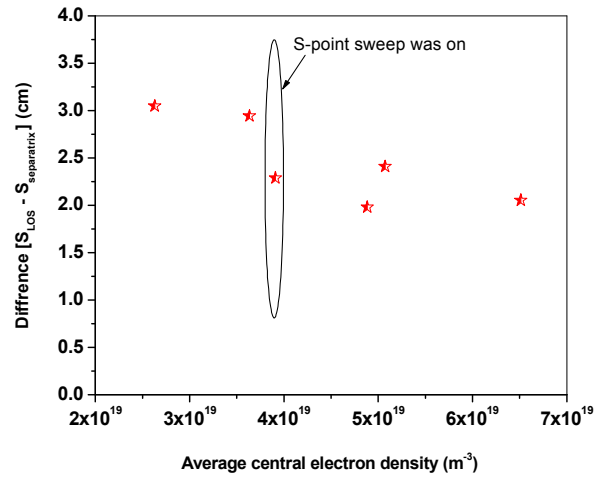


Fig.20. Difference between the strike point position and spectroscopic line-of-sight (LOS) for the ohmic series discharges

influxes of different ionizing stages of dominant species are then derived as shown for ohmic discharges in the Fig. 21. It is inferred that the deuterium and helium ground state fluxes has increased for the increasing upstream density and after certain peak value they starts decreasing. He II flux is almost unchanged. The fluxes of carbon, boron and oxygen have reduced drastically in the recombining region of the plasmas. It should be noted that the S/XB method to derive fluxes is not very appropriate to the recombining plasma cases. The decrease in the temperature causes the decrease in physical sputtering of these elements [45]. For the measured low temperature in the recombining plasmas, the physical sputtering should have become negligible. Therefore, the existence of the boron and carbon fluxes even in spite of low temperature may be due to chemical sputtering instead of physical sputtering [46] or due to the failure of S/XB method in the recombining phase. The fractional abundances of various impurity species can be easily obtained from such analysis. The measurement of fractional abundance helps in understanding local plasma equilibrium.

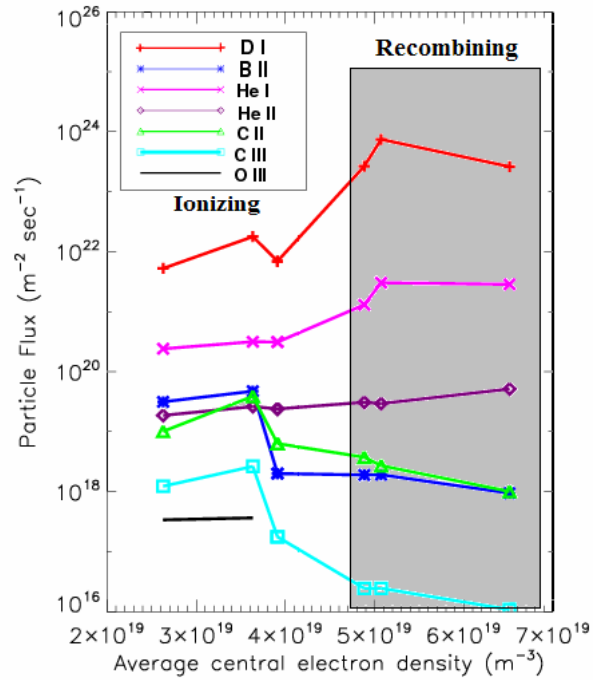


Fig.21. Particle fluxes of different ionizing states of dominant species in ohmic series discharges. The shaded region indicates recombining condition for deuterium, where the evaluation in terms of particle fluxes is not possible.

3.3 Detached Divertor Plasmas: (Conditions of Attachment and Detachment)

At low core plasma densities it is often observed that the divertor target temperature is sufficiently high ($T_t > 5$ eV) for friction processes (i.e., charge-exchange and elastic scattering) to be neglected in comparison to the ionization. In such a case the total pressure (static and kinetic) is constant along field lines and such conditions are termed as attached divertor plasmas [47]. In such a situation radiation loss processes and the flux of potential energy (which includes the ionization energy of a hydrogenic atom ~ 13.6 eV and half the binding energy of a hydrogenic molecule

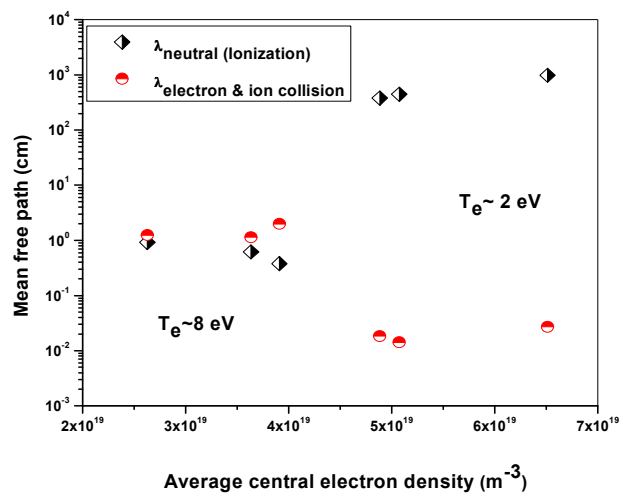


Fig.22. A plot for electron-neutral and electron-ion collisional mean free path for the discharges from table and four

$\sim 2.2\text{eV}$) are assumed to be negligible compared with the kinetic power. When plasma temperature in a divertor region is sufficiently low ($< 5\text{ eV}$) and plasma density is high, the rate of neutral ionization reduces and plasma becomes recombining (see fig. 15). Apparently the neutral mean free path increases as shown in Fig 22 for ohmic series discharge of recombining plasmas. The neutral (ionization) mean-free-path and electron-ion collision mean-free-path are calculated at the estimated electron temperatures and densities by using the thermal velocity of the neutral deuterium atoms at the room temperature (i.e., $2 \times 10^3\text{ m s}^{-1}$). Under these circumstances, the charge exchange processes in the divertor begin to dominate over ionization processes, and neutrals produced at the divertor plate have a very large probability of being scattered back to the divertor before they are ionized, which build the neutral pressure in the divertor region. In such a situation, pressure balance no longer holds across the emission region since ion momentum is lost through collisions with neutrals.

To visualize the pressure balance in AUG for the ohmic series discharges, the midplane plasma pressure at separatrix is calculated using electron density measurements from the Lithium beam diagnostic and electron temperature measurements from the Thomson scattering diagnostic. The pressure is then compared with the plasma pressure obtained from our estimated average temperatures and densities in the outer divertor region as shown in Fig. 23. It clearly shows that this effect has become increasingly significant at lower temperature values of recombining plasmas.

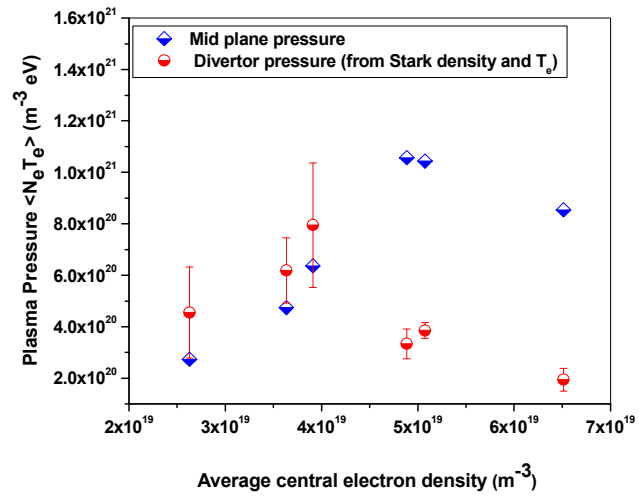


Fig.23. Comparison of the plasma pressure at midplane and divertor region

We will now consider in detail the experimental observations that characterize the divertor detachment. We plotted various particle fluxes in the outer divertor region for the increasing main plasma densities (see Fig. 24). The fluxes are derived using ion saturation current of divertor

target Langmuir probe, D_α signal from a calibrated diagnostic viewing the strike point area (SPO diagnostic), D_β and D_γ signals from Echelle spectrometer. The spectroscopic signals are converted into the particle fluxes by multiplying the D_α , D_β and D_γ absolute intensities with corresponding S/XB coefficients taken from the ADAS database. A table of the obtained S/XB values along with the corresponding photon fluxes at the estimated temperatures and densities for the ohmic series discharges is given below.

Table VI: Table of S/XB values and photonic fluxes of deuterium Blamer series lines in the ohmic series discharges

Shot No.	N_e (m ⁻³)	T_e (eV)	S/XB	S/XB	S/XB	S/XB	photons m ⁻² s ⁻¹ nm ⁻¹			
			D_α	D_β	D_γ	D_δ	D_α	D_β	D_γ	D_δ
21258	7.8×10^{19}	7.87	33	400	2249	13972	7.5×10^{20}	3.8×10^{19}	3.8×10^{18}	1.3×10^{18}
21279	6.2×10^{19}	7.33	26	305	1798	11154	3.4×10^{20}	1.7×10^{19}	3.2×10^{18}	5.3×10^{17}

21320	7.7×10^{19}	10.3	44	510	2385	14652	3.3×10^{20}	2.3×10^{19}	4.9×10^{18}	5.1×10^{17}
21322	1.2×10^{20}	1.54	12	220	1205	9653	5.4×10^{21}	3.3×10^{20}	1.2×10^{20}	4.4×10^{19}
21325	2.0×10^{20}	1.62	20	362	1978	15806	7.8×10^{21}	3.3×10^{20}	1.1×10^{20}	4.1×10^{19}
21327	2.4×10^{20}	1.56	23	417	2273	18378	1.2×10^{22}	6.9×10^{20}	2.7×10^{20}	9.6×10^{19}

It is evident in the figure that the ion fluxes obtained by the Langmuir probe increases and then start decreasing for increasing upstream density. As temperature decreases (recombining plasma situation), the number of ionizations per photon decreases, and accordingly the deuterium emissions (D_α , D_β) increase for the available ionization source [48]. The identical values of D_α and D_β flux by two different diagnostics (i.e., SPO and Echelle spectrometer) for the same viewing LOS indicate that the calibration of spectroscopic diagnostic is consistent.

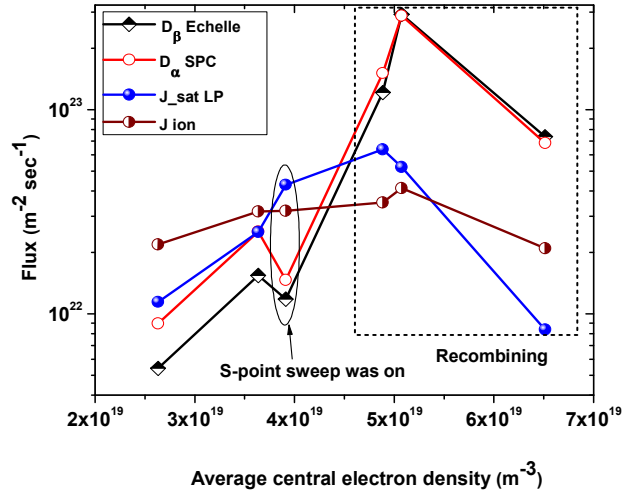


Fig.24 Comparison of various particle fluxes obtained by Echelle spectrometer, SPO diagnostics and Langmuir probe

The variation of fluxes from spectroscopy and Langmuir probe could be understood in the following way. In the process of enhanced neutral pressure during low temperature, the neutrals can carry to the target a significant fraction of the momentum of the incoming ions and, therefore, prevent the ion flux from increasing further at the divertor (see Langmuir probe flux in the adjacent figure). This process reveals decrease in the divertor ionization source and the large deuterium emissions during recombining plasmas.

The observed values of electron density and temperature from the Langmuir probe and spectroscopy are not identical. We made a comparison of the obtained plasma densities and temperatures using both diagnostics as shown in the Fig. 25. The found values are quite different. This practical difference would be due to the measurement positions. The Langmuir probe is measuring parallel fluxes along field lines whereas spectroscopy measuring line integrated signal across the divertor. The viewing geometry is shown in the Fig. 6. In order to learn the consistency in these measurements we can apply following method. From the sheath limited currents [49 and references therein], the random ion flux J_{sat} on a target can be written as,

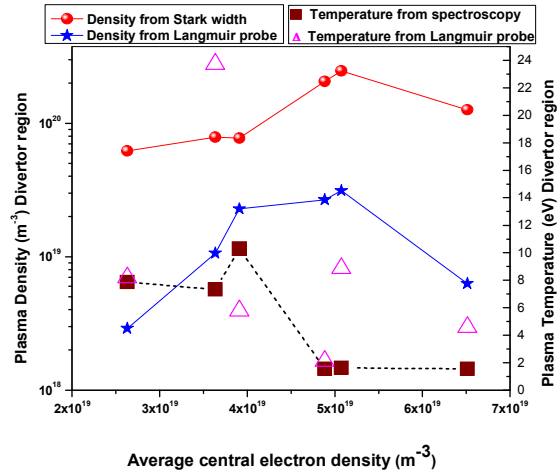


Fig.25. Comparison of the electron densities and temperatures derived by Langmuir probe and spectroscopic diagnostics

$$J_{-sat} = \frac{eN_i \langle v_i \rangle}{4} = \frac{eN_i}{4} \sqrt{\frac{8kT_i}{m\pi}} \approx 0.4eN_i \sqrt{\frac{T_i}{m}} = 0.4eN_i \sqrt{\frac{T_i}{T_e}} \sqrt{\frac{T_e}{m}} = eN_i K_0 \sqrt{\frac{T_e}{m}}, \quad (10)$$

where $K_0 = 0.4 \sqrt{\frac{T_i}{T_e}}$, $N_i \langle v_i \rangle$ is the average ion flux, T_i is the ion temperature and m is the ionic mass. The value of K_0 for $T_i \ll T_e$ is ~ 0.607 and for $T_i = T_e$ it is 0.4. By assuming the quasi-neutral isothermal plasma we can apply simple relationship,

$$J_{-sat} = 0.4eN_e \sqrt{\frac{T_e}{m}} \quad (11)$$

Now using the values of average temperatures and densities from the spectroscopic diagnostic we can calculate J_{-sat} . To convert this calculated flux as directed flux similar to the Langmuir probe (we call it ‘ion flux’ J_{ion}), the angle of field lines θ can be utilized which will finally bring the following relationship,

$$J_{ion} = 0.4eN_e \sqrt{\frac{T_e}{m}} \sin \theta \quad (12)$$

The observed value of θ for ohmic series discharges is $\sim 3^\circ$. The values of J_{ion} are shown in the Fig. 19, which reveals comparable values to Lagmuir probe. It is to be noted that the all measurements stated herein are average measurements and 20-30% error is quite likely in the projected values. This comparison of fluxes observed by different diagnostics supports the consistency of our analysis.

In order to summarize our many observations, the degree of detachment has to be obtained. Following the simple two point model of the divertor plasma [50] and the assumption of square law dependency of the main plasma density, the extrapolated ion flux to the divertor can be written from the well-known [51] relationship,

$$J_d^{scale} = C \langle \tilde{N}_e \rangle^2 \quad (13)$$

where J_d^{scale} is the extrapolated ‘attached’ divertor ion flux, C is the normalized constant and $\langle \tilde{N}_e \rangle$ is the main plasma density. Under simple approximation the main plasma density will be proportional to the separatrix density $\langle \tilde{N}_e \rangle_{sep}$ and the extrapolated ion flux will be given by,

$$J_d^{scale} = C \langle \tilde{N}_e \rangle_{sep}^2 \quad (14)$$

On the basis of this very simple scaling, the degree of detachment is defined as [51],

$$DOD = \frac{J_d^{scale}}{J_{sat}^{measured}} \quad (15)$$

where $J_{\text{sat}}^{\text{measured}}$ is the measured ion flux by the Langmuir probe. A logarithmic plot for $I_{\text{d}}^{\text{scale}}$ and $J_{\text{sat}}^{\text{measured}}$ is shown in the Fig. 26. The dotted line represents the $I_{\text{d}}^{\text{scale}}$ values obtained by keeping the slope of logarithmic values of raising ion flux from Langmuir probe and $\langle \tilde{N}_e \rangle_{\text{sep}}$ equal to two. The degree of the detachment in the ohmic series is highlighted in the graph. The detached plasmas are identified when the degree of detachment becomes notably larger than unity. The degrees of detachment shown indicate that we have achieved detached plasma in the ohmic series discharges.

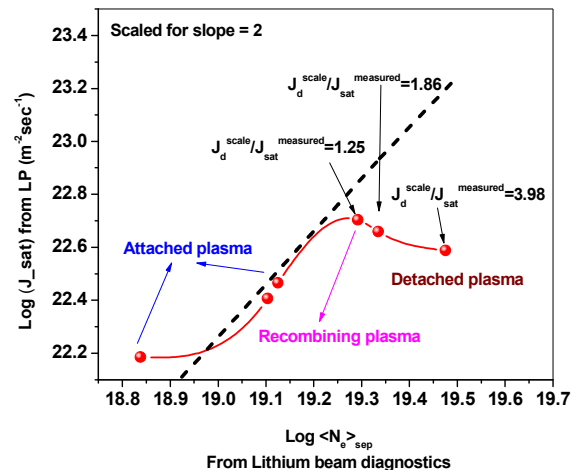


Fig.26. A logarithmic value plot of the ion fluxes from Langmuir probe for increasing separatrix density $\langle \tilde{N}_e \rangle_{\text{sep}}$

When the plasma detaches away from the divertor target, the radiation moves towards the confined plasma and the divertor density starts decreasing (see Fig. 25). The decrease in plasma density and temperature under such condition cause a decrease in the conducted power across the sheath. Hence, low plasma power reaches the material surface during the detachment. Due to this reason, detached plasmas are considered the key answer to the problem of reducing peak power loads to the divertor target in a fusion reactor.

4. Discussion:

To ascertain our density estimation using Stark profile evaluation it is important to understand various broadening mechanisms. In fact, the measured profile of an emission line can be affected by different mechanisms of broadening: natural broadening, Doppler broadening (due thermal effects), Stark broadening (due to collisional effects), and also instrumental broadening (due to slit width) etc. In general, the important broadening mechanism generates Gaussian profiles, except the Stark broadening. The Stark broadening with full-width-half-maxima (FWHM) $\Delta\lambda_S$ is determined by the electron density. The Doppler broadening gives Gaussian profile with width $\Delta\lambda_D$ which depends on background species temperature. Since spectrometers are insensitive to distinguish different line shapes, the convolution of Stark and Gaussian profiles is important to interpret the results. Using zeroth order simplification people assume that the Stark profile is similar to Lorentzian profile [41-42]. With this simplification it becomes possible to de-convolute the Lorentzian (Stark) part from the spectral line using Voigt fit procedure [52].

The Voigt profile in the wavelength scale in units of Gaussian line-shape half-width $\alpha_G = \Delta\lambda_G/2$ and Lorentzian line-shape half-width $\alpha_L = \Delta\lambda_L/2$ is given by,

$$\phi(\lambda) = \frac{1}{\alpha_G} \sqrt{\frac{\ln 2}{\pi}} K(a, u) \quad (16)$$

where $K(a, u)$ is the Voigt function and is known as

$$K(a, u) = \frac{a}{\pi} \int_{-\infty}^{\infty} \frac{e^{-y^2} dy}{a^2 + (u - y)^2}, \quad (17)$$

by having
$$a = \frac{\alpha_L}{\alpha_G} \sqrt{\ln 2}, \quad (18)$$

and
$$u = \frac{\lambda - \lambda_0}{\alpha_G} \sqrt{\ln 2}. \quad (17)$$

Using above relationship, from equation (14)-(17), an IDL based fit program is developed. We can obtain the best fit half-width values of α_G and α_L , and correspondingly FWHM's of the Doppler and Lorentz widths for the D_δ and D_γ lines. The instrumental width is obtained using a Chromium lamp at the most closer wavelength to the Balmer series deuterium delta line. The convolved Gaussian and Lorentzian widths in instrumental width are 0.024 nm and 0.0028 nm respectively. It is apparent that the most part of the instrumental width is Gaussian in nature. The actual Doppler and Lorentz FWHM's are then calculated using the following relationship,

$$\Delta\lambda_D (\text{Doppler}) = \sqrt{[(\Delta\lambda_{G(\text{Expt})})^2 - (\Delta\lambda_{G(\text{Instr})})^2]} \quad (19)$$

and
$$\Delta\lambda_L (\text{Lorentz}) = (\Delta\lambda_{L(\text{Expt})}) - (\Delta\lambda_{L(\text{Instr})}) \quad (20)$$

where $\Delta\lambda_{G(\text{Instr})}$ and $\Delta\lambda_{L(\text{Instr})}$ signifies the part of the FWHM's of Gaussian and Lorentzian line-shapes in an instrumental width. While $\Delta\lambda_{G(\text{Expt})}$ and $\Delta\lambda_{L(\text{Expt})}$ denotes the obtained actual FWHM's of Gaussian and Lorentzian line-shapes from the experiment.

The Voigt FWHM is given by

$$\Delta\lambda_V (\text{Voigt}) = \sqrt{[(\Delta\lambda_L / 2)^2 + (\Delta\lambda_G)^2]} + (\Delta\lambda_L / 2). \quad (21)$$

Once we convolve the Lorentzian part of the spectral line and assume $\Delta\lambda_L (\text{Lorentz}) = \Delta\lambda_S$, the electron density from the Stark broadening can be estimated by the GKS theory [53] in a quasi-static approximation using the classical Holtsmark's normal field strength as,

$$N_e = \left[\frac{\Delta\lambda_S (\text{Stark}) \times 10^9}{2.508 \alpha_{1/2}} \right]^{3/2} \times 10^6 \quad (22)$$

where $\Delta\lambda_S (\text{Stark})$ is the FWHM of the Stark width, N_e is the electron density and has units of m^{-3} . The fractional semi-half-width parameter $\alpha_{1/2}$ is tabulated in reference [32] in the form of discrete data points for different electron temperatures and densities which has units of \AA . The tabulated data covers values of $\alpha_{1/2}$ for low plasma temperatures only. Using Stehle *et al.* [16] code we have derived $\alpha_{1/2}$ values for higher temperatures as

shown in Fig. 27 for D_δ line. In the domain of our density interest, the effect of temperature on $\alpha_{1/2}$ is quite weak.

Density analysis using Voigt fit (for # 21258) is shown in Fig.28. This estimated density lies within the error limit of our previous density measurement (see Fig. 14). The purpose of this approximated analysis was simply to make out the influence of the Doppler broadening on the estimated densities because we have averaged out T_{eff} which is responsible for the Doppler broadening exclusively caused by the instrument and thermal background species (see section 3.1.1). The identical values of two estimated densities indicate that without going into the details of convolution procedure the procedure of averaging T_{eff} is adequate.

The Voigt fit procedure becomes more erroneous when one measures high density plasmas because far wings of the D_δ and D_γ lines start expanding. In such cases, Lorentzian and Stark profile will deviate very much at the far wings and obviously the half-width (see Fig. 29 a and b). Therefore, the assumption of identical profiles will introduce more uncertainty in the density estimation because the Stark broadening is mainly determined by the wings of the profile [16]. A comparison of our numerical fit and the Voigt fit procedure to the experimental D_δ line is shown in Fig. 30. In this comparison the obtained Gaussian width from the Voigt fit was converted in to the T_{eff} by utilizing the

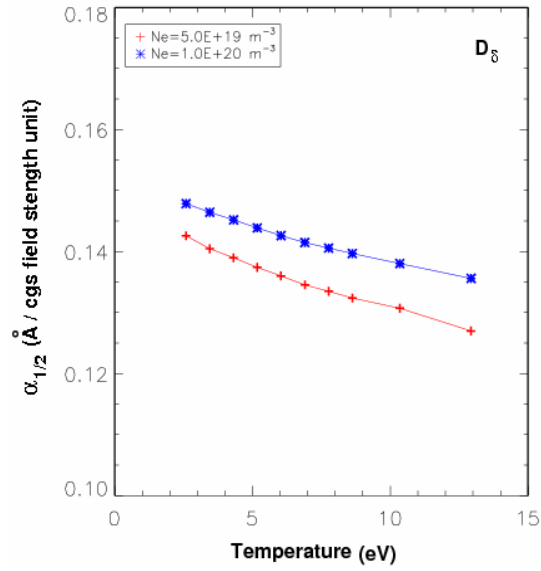


Fig.27. Variation of fractional semi-half-width parameter $\alpha_{1/2}$ with electron temperature and density

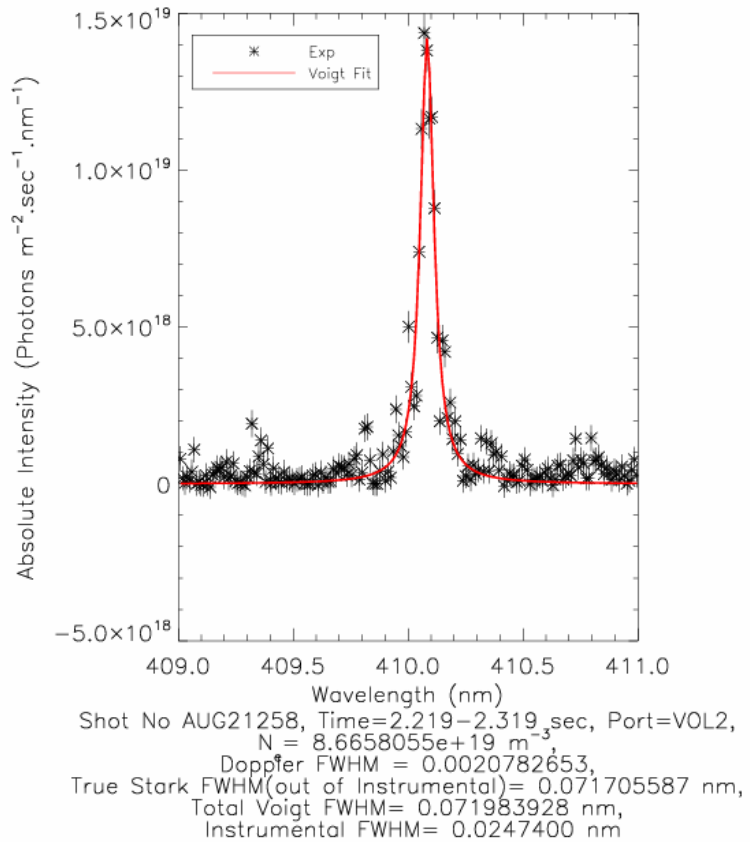


Fig.28. Density estimation by Voigt fit procedure

temperature dependency of the Doppler width and then a combined profile of Gaussian and Stark is generated from Stehle *et al.* [16] tabulation code. The comparisons of

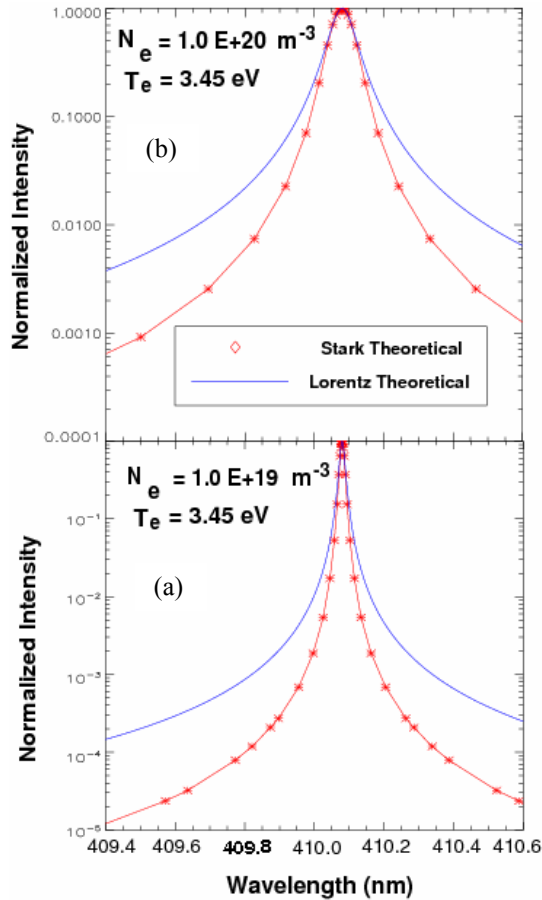


Fig.29. Theoretical Lorentzian and Stark profiles of D_δ line at a fixed temperature and different densities

experimental, the Voigt fit and this tabulation code profiles shows deviation at the wings for Voigt fit. The assumption of Lorentzian profile as Stark profile is, therefore, not accurate.

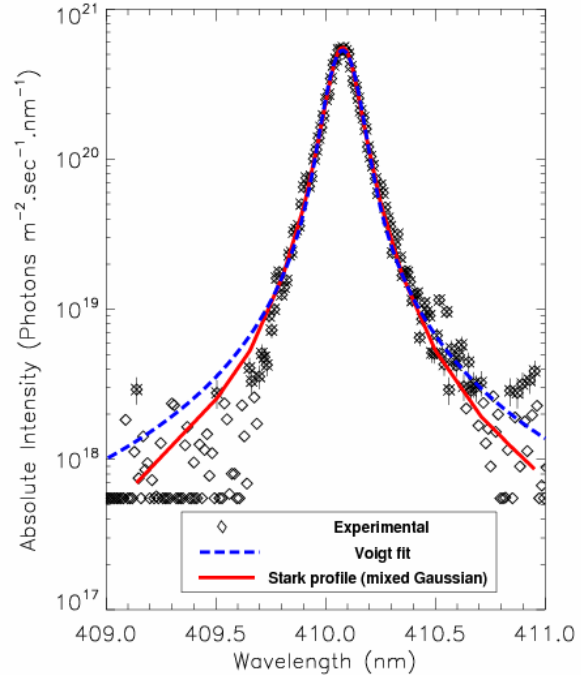


Fig.30. Comparison of numerical Stark fit and the Voigt fit procedure with experimental D_δ line

5. Conclusions:

The divertor region plasma of ASDEX Upgrade tokamak has been characterized using an Echelle spectrometer and various spectroscopic codes. A table of the identified wavelengths from the obtained large wavelength range spectrum of Echelle spectrometer is prepared. The observed spectral lines indicate that the main impurities present in the divertor plasma are boron, helium, carbon and oxygen with different ionizing stages. A couple of nitrogen, molybdenum, argon and calcium lines are also observed. The observation of CD, BD 0-0 and BD 1-1 molecular band is reported.

The purpose of this study was to establish spectroscopy based plasma parameter diagnostic and accordingly the impurity influx measurements in the divertor region plasma. Using Stark broadening tabulations by Stehle *et al.* [16] for deuterium Balmer series δ and γ lines it became possible to estimate average plasma densities. We have developed a chi-square fit procedure with the experimentally measured D_δ line using known profiles of the tabulation code. The values of chi-square minimize for certain

densities. To estimate plasma densities from this fit procedure a probability analysis is carried out. The peak of the probability distribution function gives us the density values whereas its half-width determines preliminary errors on the estimations. Since D_γ line shows significant Stark broadening and is equally useful for density measurements, the relative uncertainties are calculated by comparing obtained estimated density values of D_δ with D_γ line.

With a view to identify useful temperature diagnostics in the divertor region, the ADAS database is explored to identify the absolute line intensities and the ratios of spectral lines of different species. The calculation of the excited state populations of the ion of interest is the necessary precursor to such examinations. From these, the line intensities and their ratios as function of temperature and density can be calculated for easy comparison with experimental observations. We have used full CR-model and a chi-square minimization method for determining simultaneously the effective electron temperature, average ground state atoms and ions column densities from the number of spectral lines of a single ionizing species at the estimated average plasma densities. The proposed method includes self-consistent uncertainties on the estimated values.

The boron line ratios BII 703.20 (triplet) / B II 419.48, B II 412.19/ B II 628.7 and B II 447.21(triplet)/ B II 419.48 are identified temperature sensitive under the ionizing plasma conditions and can be utilized to find effective plasma temperature in the divertor region. In cases where boron lines are not prominent, a temperature and density sensitive helium line ratio [He I 667.8/ He I 706.57] can be employed by introducing density as input from the Stark broadening calculations. The reported line ratios are suitable for ionizing plasmas. A comparison of the two methods in the ionizing plasma cases gives identical temperature values whilst for recombining plasmas the comparison of ionizing ratios with full CR-model does not match. With onset of recombination, a clear disagreement is observed, putting strong doubts on the applicability of the line ratio method under divertor conditions.

On the basis of estimated basic plasma parameters and subsequent S/XB values derived from ADAS code, the impurity influx measurements for ohmic series discharges have been carried out. During recombining phase, helium ground state and deuterium fluxes are increased compared to the ion fluxes at the target. Moreover the fluxes of boron and carbon have reduced drastically. The sudden reduction of electron temperature leads negligible physical sputtering and hence the presence of these fluxes could be due to the chemical sputtering. A comparison of the ion fluxes obtained by various diagnostics is made in the outer divertor region which satisfies our quantitative analysis.

Observations of detached and attached plasmas are reported for ohmic series discharges. The plasmas are attached with higher temperature $\sim 7-10$ eV under ionizing condition. Detached plasmas are found at quite low temperature ~ 2 eV during recombination process. The recombination is observed in the line ratios of deuterium Balmer series lines. The stated maximum degree of detachment for ohmic series discharges is ~ 4 .

Bibliography

1. W. Koppendorfer, M. Blaumoser, H. Bruhns, C. Dorn, J. Gernhardt, *et al.*, Completion of Assembly and Start of Technical Operation of ASDEX Upgrade, in *Fusion Technology (Proc. of the 16th Symposium on Fusion Technology, London, U.K., 1990)*, edited by B. Keen, M. Huguet, and R. Hemsworth, **volume 1**, pages 208-212, Amsterdam, 1991, Elsevier.
2. ITER-Homepage, "<http://www.iter.org>".
3. R. Aymar, V. Chuyanov, M. Huguet, Y. Shimomura, and ITER Joint Central Team and Home Teams, *Nucl. Fusion* **41**, 1301-1310 (2001).
4. ITER physics basis editors, *Nucl. Fusion* **39**, 2137-2638 (1999).
5. R. Neu, *IPP-Report*, **IPP 10/25** (2003). [and reference therein]
6. D. R. Bates, A. E. Kingston, and R. W. P. McWhirter, *Proc. Roy. Soc.* **A257**, 297 (1962).
7. ADAS Homepage, "<http://adas.phys.strath.ac.uk/>".
8. H. P. Summers, Atomic data and analysis structure users manual, **JET-IR 06** (Abingdon: JET Joint Undertaking) (1994).
9. R. A. Hulse, "The ALADDIN atomic physics database system", Atomic processes in plasmas, *AIP conf. Proc.* **206** (Edited by Y. K. Kim and R. C. Elton)(American Institute of Physics, New York, 1990), p. 63.
10. Dare K.P., Landi E., Mason H.E., Monsignori Fossi B. and Young P.R., *Astro. Suppl. Series*, **125**, 149 (1997).
11. A. S. Kukushkin *et al.*, 17th *Fusion Energy Conference, October 19 – 24, Yokohama, Japan, ITERP1/13, IAEA-CN-69* (1998).
12. The ASDEX Team, *Nucl. Fusion* **29**, 1959 (1989).
13. J. L. Terry, B. Lipschultz, A. Yu. Pigarov, S. I. Krasheninnikov, B. LaBombard, D. Lumma, H. Ohkawa, D. Pappas, and M. Umansky, *Phys. of Plasmas*, **5**, 1759-1766 (1998).
14. U. Wenzel, *et al.*, *Nucl. Fusion*, **39**, 873-882 (1999).
15. R. H. Huddlestone and S. L. Leonard, Eds., "*Plasma Diagnostic techniques*", New York: Academic, (1965).
16. C. Stehle and R. Hutcheon, *Astron. Astrophys. Suppl. Ser.* **140**, 93-97 (1999).
17. U. Frisch and A. Brissasud, *J. Quant. Spectrosc. Rad. Transfer* **11**, 1753 (1971).

18. Ram Prakash, P. Vasu, Vinay Kumar, R. Manchanda, and M. B. Chowdhuri, *J. Appl. Phys.* **97**, 43301, (2005).
19. M. E. Fenstermacher *et al.*, *Plasma Phys. Control. Fusion* **41**, A345–A355 (1999).
20. <http://www-drfc.cea.fr/gb/fusion/physique/>
21. M Bécoulet *et al.*, *Plasma Phys. Control. Fusion* **45** A93-A113 (2003).
22. A. Sips, J. Hobirk, and A. G. Peeters, *Fusion Sc. & Tech.*, **40**, 605 (2003).
23. D.A. Skoog, F.J. Holler and T.A. Nieman, *Principles of instrumental analysis, Florida, Harcourt Brace & Company* (1998).
24. J.V. Sweedler, *CRC Crit. Rev. Anal. Chem.*, **24**, 59-98 (1993).
25. J.M. Harnly, R.E. Fields, *Appl. Spectrosc.*, **51**, 334A-351A (1997).
26. NIST Physical Reference data <http://physics.nist.gov/PhysRefData/ASD/>
27. R. Brandenburg *et al.*, *Fusion Sc. & Tech.* **36**, 289-295 (1999).
28. B. Kurzan, H. Murmann, H. Salzmann, and ASDEX Upgrade Team *Rev. of Sc. Instrum.* **72**, 1111-1114 (2001).
29. H.W. Müller *et al.*, *Nucl. Fusion* **42(3)**, 301-309 (2002).
30. K. Behringer, 'Description of the impurity transport code STRAHL', *JETR(87)08*, *JET Joint Undertaking, Culham* (1987).
31. R. Dux, STRAHL User Manual, *IPP 10/30* (2006).
“www.ipp.mpg.de/ippcms/de/kontakt/bibliothek/ipp_reports/IPP_10_30.pdf”
32. H. R. Griem, *Spectral Line Broadening by Plasmas*, 282–296 (*Academic, New York*, 1974).
33. L. L. Wiese and J. A. Augis, *J. Appl. Phys.* **48**, 4528–4535 (1977).
34. V. Helbig and K. P. Nick, *J. Phys. B* **14**, 3573–3583 (1981).
35. H. R. Griem, *Phys. Rev.* **A28**, 1596–1601 (1983).
36. J. Ashkenazy, R. Kipper, and M. Caner, *Phys. Rev. A* **43**, 5568–5574 (1991).
37. C.R. Vidal, J. Cooper and E. W. Smith, *Astroph. J. Suppl.* **25**, 37-135 (1973).
38. H. Ehrich and D. E. Kelleher, *Phys. Rev. A* **21**, 319–334 (1980).

39. M. A. Gigosos and V. Cardeñoso, *J. Phys. B: At. Mol. Opt. Phys.* **29**, 4795-4838 (1996).
40. H. Griem, *Principles of Plasma Spectroscopy*, Cambridge Univ. Press (1997).
41. D. P. Stotler, C. H. Skinner and C. F. F. Karney, *Rev. Sci. Instrum.* **70**, 347 (1999)
42. J. Torres et al., *J. Phys. D: Applied Phys.* **36**, L55-L79, (2003).
43. T. Fujimoto, *J. Quant. Spectrosc. Radiat. Transfer.* **21**, 439 (1979).
44. U. Samm, *Trans. of Fusion Tech.* **33**, 338 (1998).
45. D. G. Whyte *et al*, *Nuclear Fusion*, **41**, 1243 (2001).
46. J. Roth, *J. Nucl. Mater.* **266-269**, 51-57 (1999).
47. G. F. Matthews, *J. of Nucl. Materials*, **220-222**, 104-116 (1995).
48. Y. R. U. Andrew, *thesis (University of London)* (1999).
49. U. Deka, Ram Prakash, A. Sarma and C. B. Dwivedi, *Jpn. J. of Appl. Phys.* **43**, 2704 (2004).
50. M. Keihacker *et al.*, *Phys. Scr.*, **T2/2**, 443 (1982).
51. A. Loarte *et al.*, *Nucl. Fusion*, **38**, 331-371 (1998).
52. B. H. Armstrong and R. W. Nicholls, “*Emission, Absorption and Transfer of Radiation in Heated Atmospheres*”, Pergamon Press, Oxford (1972).
53. P. Kapple and H. R. Griem, *Phys. Rev.* **173**, 317 (1968).